











Tonian Continental Arc Magmatism of the Porongos Complex, Dom Feliciano Belt, Southern Brazil

*Magmatismo Toniano de Arco Continental do Complexo
Porongos, Cinturão Dom Feliciano, Sul do Brasil*

Rodrigo Antonio de Freitas Rodrigues¹ , Juliana Pertille² , Fernanda Gervasoni¹ , Paola Bruno Arab³ ,
Thales Sebben Petry⁴ , Marina Luiza Jordão Martins⁵ , Áquila Ferreira Mesquita⁶ ,
Jorge Henrique Laux⁷ , Breno Souza Martins⁸ , Lívia Brochi Nascimento⁸ 

¹Universidade Federal de Pelotas, Centro de Engenharias, Rua Benjamin Constant, 989, CEP: 96010-020, Pelotas, RS, BR
(rodrigues.rafr@gmail.com; gervasoni.fe@gmail.com)

²Universidade Federal de Pelotas, Centro de Desenvolvimento Tecnológico, Programa de Pós-Graduação de Recursos
Hídricos, Pelotas, RS, BR (juliana.pertill@gmail.com)

³Universidade Federal de Goiás, Faculdade de Ciências e Tecnologia, Goiânia, GO, BR (paola.arab@gmail.com)

⁴Universidade Federal do Rio Grande do Sul, Programa de Pós-Graduação em Geociências, Porto Alegre, RS, BR
(thales_petry@hotmail.com)

⁵Universidade do Vale do Rio dos Sinos, São Leopoldo, RS, BR (marinaljm@edu.unisinos.br)

⁶Universidade Estadual de Campinas, Instituto de Geociências, Departamento de Geologia e Recursos Naturais, Campinas, SP,
BR (aquila.fmesquita@gmail.com)

⁷Serviço Geológico do Brasil, Porto Alegre, RS, BR (jorge.laux@sgb.gov.br)

⁸Universidade Federal de Uberlândia, Instituto de Geografia, Monte Carmelo, MG, BR (brenosouzamartins@yahoo.com.br;
liviabrochi@live.com)

Received on February 12, 2023; accepted on May 31, 2023.

Abstract

This study provides new information on the deformation, metamorphism, and tectonic setting of the metavolcanic rocks of the southern portion of the Porongos Complex, southern Brazil. The structural analysis enabled the identification of three deformational phases, formed under ductile to semi-ductile conditions. D₁ progressed through deformation partitioning, comprising closed to isoclinal folds and an axial plane foliation. Then, simple shear prevailed, resulting in isoclinal folds, sigma-type porphyroclasts, foliation transposition, and mylonitic rocks. D₂ comprises open to gentle folds and an axial plane cleavage. The formation of shear bands is ascribed to the semi-ductile D₃. The mineral assemblage represented by phengite + chlorite + clinozoisite-epidote + actinolite + albite + quartz associated with the temperatures obtained through the chlorite geothermometer (316°C) indicates greenschist facies conditions. The protoliths of these metavolcanic rocks are geochemically discriminated as calc-alkaline, dacite-to-rhyodacite, with peraluminous compositions. The bulk trace element compositions show enrichment in large-ion lithophile elements and light rare-earth elements and depletion in heavy rare-earth elements. Also, negative Nb, P, Ti, and Ta anomalies are observed in the multielement diagram. All these geochemical features are typical of rocks formed in continental magmatic arcs. Geochemical comparison with other pre-collisional Tonian orthometamorphic rocks from the Dom Feliciano Belt demonstrates strong similarities, which corroborates the prior interpretation of a continental arc setting for the origin of these Tonian rocks.

Keywords: Tonian Magmatism; Continental Magmatic Arc; Porongos Metamorphic Complex; Fold and Thrust Belt; Metavolcanic Rocks.

Resumo

Este estudo apresenta novas informações sobre deformação, metamorfismo e ambiente tectônico das rochas metavulcânicas da porção sul do Complexo Porongos, sul do Brasil. A análise estrutural permitiu a identificação de três fases de deformação, formadas sob condições dúcteis a semidúcteis. D₁ progrediu por meio de partição da deformação, compreendendo dobras fechadas a isoclinais e uma foliação plano axial. Nesse estágio, prevalece o cisalhamento simples, resultando em dobras isoclinais, porfiroclastos do tipo sigma, foliação de transposição e rochas miloníticas. D₂ compreende dobras abertas a suaves e uma clivagem plano axial. A formação de bandas de cisalhamento é atribuída à fase semidúctil D₃. A assembleia

mineral representada por fengita + clorita + clinozoisita-epidoto + actinolita + albita + quartzo associado às temperaturas obtidas por meio do geotermômetro de clorita (316 °C) indicam condições de fácies xisto verde. Os protólitos dessas rochas metavulcânicas são geoquimicamente discriminados como cálcio-alcalinos, dacito a riodacito, com composições peraluminosas. As composições de elementos traços em rocha total mostram enriquecimento em elementos litófilos de grande raio iônico (LILE) e elementos terras raras leves (LREE) e depleção em elementos terras raras pesadas (HREE). Também foram observadas anomalias negativas de Nb, P, Ti e Ta. Todas essas características geoquímicas são típicas de rochas formadas em arcos magmáticos continentais. A comparação geoquímica com outras rochas ortometamórficas tonianas pré-colisionais do Cinturão Dom Feliciano demonstra fortes semelhanças, o que corrobora a interpretação de ambiente de arco continental para a origem dessas rochas tonianas.

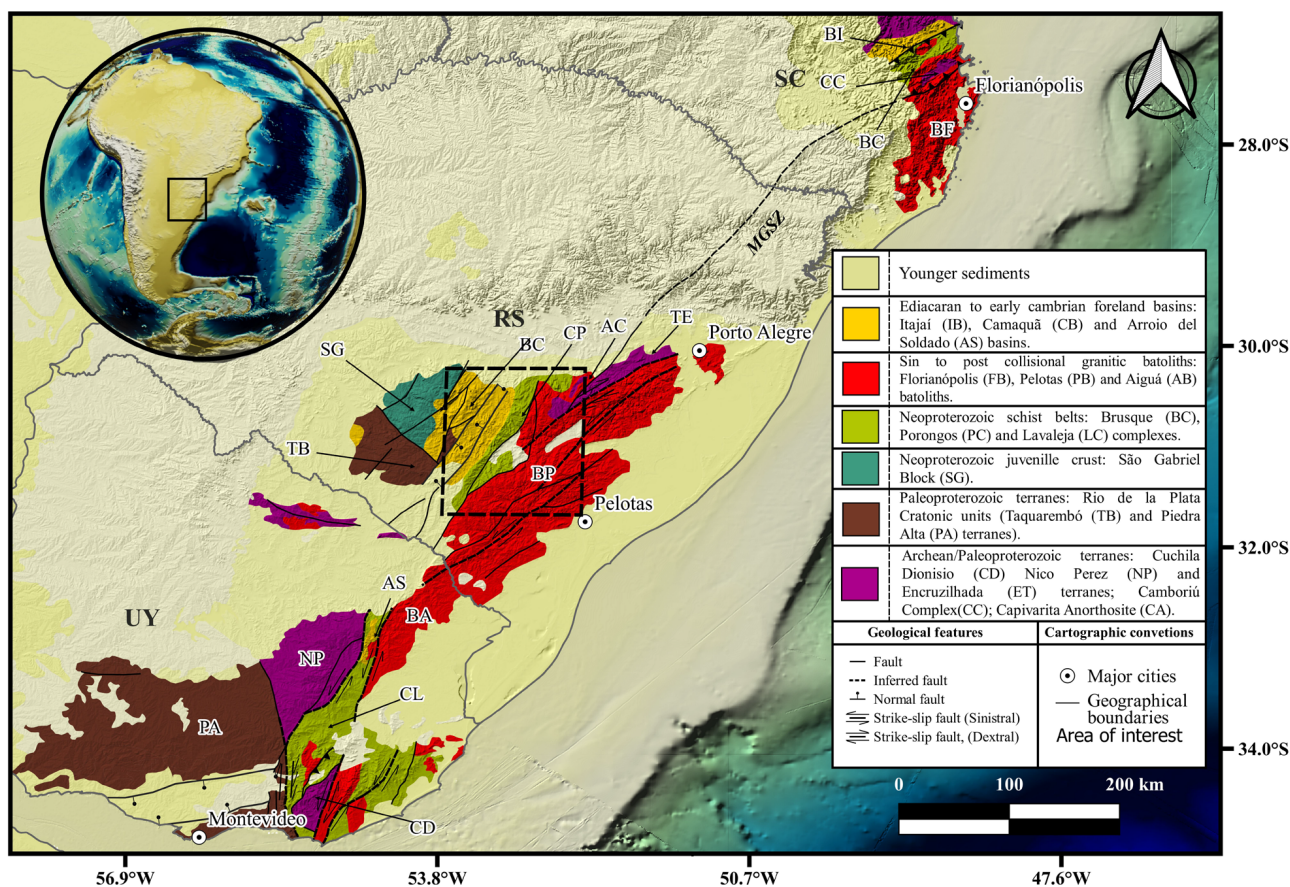
Palavras-chave: Magmatismo Toniano; Arco Magmático Continental; Complexo Metamórfico Porongos; Cinturão de Dobramento e Empurrão; Rochas Metavulcânicas.

INTRODUCTION

The assembly of the West Gondwana led to the development of several collisional episodes between cratonic nuclei with the concurrent formation of orogenic belts (Brito Neves et al., 2014; Oriolo et al., 2017). The Mantiqueira Province records significant processes of this amalgamation during the Neoproterozoic Brasiliano/Pan-African cycle

(Almeida et al., 1981). The meridional portion of this province is represented by the Dom Feliciano Belt (DFB), which is exposed for 1,200 km along southern Brazil (Santa Catarina and Rio Grande do Sul states) and Uruguay (Figure 1).

Recent studies on the DFB highlight the significance of a Tonian magmatism related to the Piratini orogeny (Lenz et al., 2011, 2013; Koester et al., 2016; Tambara et al.,



Source: modified from Takehara and Laux (2019).

Figure 1. Geological map of the Sul-Riograndense shield with the main units of the Dom Feliciano Belt.

2019; Vieira et al., 2019). For instance, geochronological and geochemical studies of the Piratini orthogneiss (Silva et al., 1999; Tambara et al., 2019), Chácara das Pedras orthogneiss (Philipp and Campos, 2004; Koester et al., 2016), Cerro Bori orthogneiss (Lenz et al., 2011, 2013), Várzea do Capivarita (VC) orthogneiss (Martil et al., 2011, 2017), and the metavolcanic rocks of the Porongos Complex (PC) (Battisti et al., 2018) interpreted these Tonian units as relics of this ancient orogeny, formed in a magmatic arc. Thus, these relicts could be products of the closure of the Charrua paleo-ocean between 780 and 650 Ma (Tambara, 2015; Ramos et al., 2018; Vieira et al., 2019). However, the timing, extension, and significance of the orogenies of DFB remain a debatable issue, particularly those of the Tonian age due to the dismembered character and overprinting of the events.

In the context of DFB, the PC is a Fold and Thrust Belt that records deformation and metamorphic processes resulting in a complex framework (Figure 2). The metavolcanic rocks, mostly metarhyolites, metadacites, and metatuffites (e.g., Saalman et al., 2006; Battisti et al., 2018) of Tonian age (Pertille et al., 2017) have been attributed to distinct tectonic scenarios. Previous works had assigned the origin of these volcanic rocks either to rift (Saalman et al., 2006, 2011; Höfig et al., 2018) or magmatic arc (Gruber et al., 2016; Martil et al., 2017; Battisti et al., 2018) settings. Therefore, the tonian magmatism of the DFB is still controversial and the origin and evolution of the volcanic rocks require thorough studies.

This study aimed to provide the first characterization of the metavolcanic rocks of the Passo da Cuia riverbed, western flank of the Godinho antiform, in the central-western portion of the Porongos Complex (Figure 2). The integration of the new data set with those previously available in the literature contributes to a better understanding of the deformational phases, metamorphism, and tectonic setting of the metavolcanic rocks during the Tonian.

GEOLOGICAL SETTING

In southern Brazil, four major orogenic events related to the Brasiliano Cycle are identified in the geological timeframe: Passinho, São Gabriel, Dom Feliciano (Leite et al., 1998; Saalman et al., 2011; Philipp et al., 2016), and Piratini (Fragoso-César, 1991; Vieira et al., 2019). The Brasiliano events reworked the Rio de La Plata Craton and its fragments, mostly originated by the Trans-Amazonian Cycle (Philipp et al., 2008; Lusa et al., 2010; Saalman et al., 2006, 2011). These fragments are spread along five crustal terranes. The oldest terrane is Taquarembó, followed by the juvenile São Gabriel, Tijucas, and the granitic Pelotas Batholith (Figure 1).

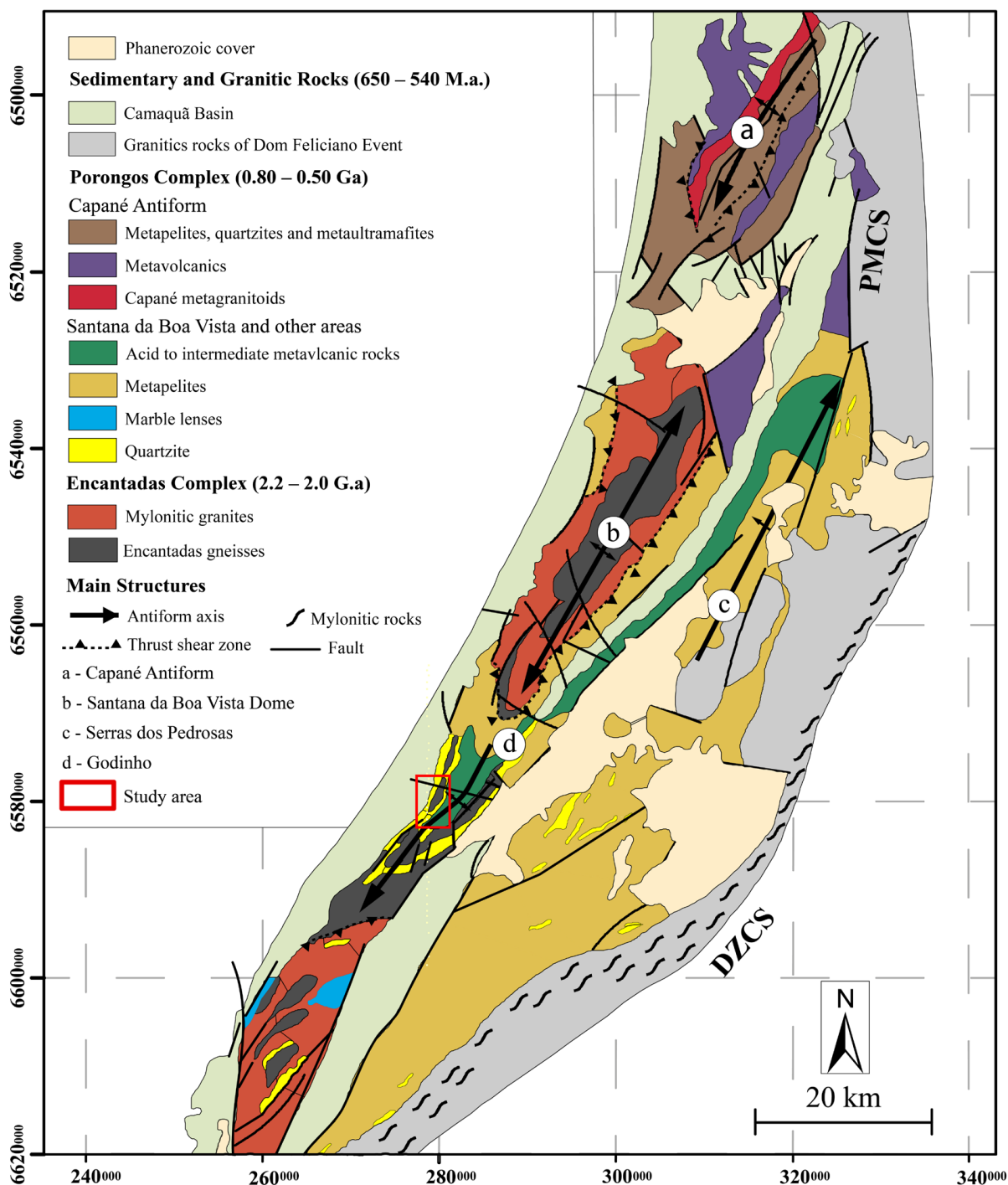
The Porongos Complex, the focus of this study, is part of the Tijucas terrane and is mainly composed of schists, quartzites, meta-arkoses, and felsic to intermediate metavolcanic rocks, as well as subordinate marble and lenses of serpentinite (Jost and Bitencourt, 1980; Porcher and Fernandes, 1990; Gollmann et al., 2008; Pertille et al., 2015a, 2015b, 2017) (Figure 2). The Paleoproterozoic basement of these rocks is the Encantadas Complex, which consists of TTG orthogneisses and mylonitic syeno- and monzogranites (e.g., Philipp et al., 2008; Lusa et al., 2010), formed during the Trans-Amazonian Cycle (2.2–2.0 Ga, Santos et al., 2003).

Four regional-scale antiforms are distinguished throughout the Porongos Complex, formed in a late ductile-brittle condition (Jost and Bitencourt, 1980; Porcher and Fernandes, 1990). From the north to the south, the regional antiforms are named as follows: Capané, Serra dos Pedrosas, Santana, and Godinho (Jost and Bitencourt, 1980) (Figure 2). The structural evolution of the PC comprises several deformation phases related to the Brasiliano Cycle, described by Saalman et al. (2006) as four ductile phases (D_1 – D_4) and one later semi-ductile to brittle episode (D_5). The metamorphic conditions of the supracrustal rocks vary from greenschist to amphibolite facies (Jost and Bitencourt, 1980; Remus et al., 1991; Fernandes et al., 1992; Porcher, 1992), reaching higher metamorphic conditions in the eastern portion of the complex (Jost and Bitencourt, 1980).

MATERIALS AND METHODS

The metavolcanic rocks of the Godinho antiform are commonly weathered. However, a small area along the Passo da Cuia riverbed of approximately 3 km² was selected for this study due to its preserved character. Structural data were collected in the fieldwork and later analyzed with the Stereonet software (Allmendinger et al., 2012; Cardozo and Allmendinger, 2013). Thirty fresh and representative samples were selected for thin-section preparation. For the petrography, we used a petrographic microscope at the Universidade Federal de Pelotas (UFPel).

After careful evaluation, seven representative samples were selected for mineral chemistry analyses. Major element concentrations of feldspars, mica, epidote, chlorite, titanite, and ilmenite were measured using a JEOL JXA-8900 Electron Probe Micro Analyzer (EPMA) equipped with five wavelength-dispersive spectrometers at the Laboratório de Microsonda Eletrônica, Instituto de Geociências, Universidade de Brasília (IG/UnB), Brazil. The analytical conditions were an acceleration voltage of 15 kV, a beam current of 15 nA, and a beam diameter of 1 μm in the spot mode. The counting time of each element during the mineral analysis was 10 s on the peak and 5 s on the background. Standards used for the quantitative measurements were



Source: modified from Philipp et al. (2016).

Figure 2. Geological map of the Porongos Complex and Encantadas Complex and the four regional antiforms.

andradite (Ca and Fe), albite (Na), forsterite (Mg), topaz (F), microcline (K, Al, and Si), vanadinite (Cl and V), pyrophanite (Ti and Mn), chromite (Cr), and nickel oxide (Ni). Matrix effects were controlled using an in-house ZAF correction program.

Whole-rock major and trace element compositions of nine representative metavolcanic rocks were obtained at the ACME Analytical Laboratories Ltd., in Vancouver, Canada (Bureau Veritas Commodities Canada Ltd.). Samples were crushed, split, and pulverized to 200

meshes. In a furnace, 0.2 g of rock powder was mixed with $\text{LiBO}_2/\text{Li}_2\text{B}_4\text{O}_7$ and fused in platinum crucibles. Each fused bead (sample) was dissolved in HNO_3 to be analyzed with the ICP-ES (Inductively Coupled Plasma Emission Spectrometry) to determine the major elements and with ICP-MS (Inductively Coupled Plasma Mass Spectrometry) to determine the trace elements. The limits of detection for major elements are between 0.002 and 0.01%, and for the most trace elements, the limits of detection range between 0.01 and 1 ppm, except for Ba, Nb, Sr, Y, Zr (2–5 ppm), V (8 ppm) Ni, Ce, and Co (20–30 ppm). The loss on ignition (LOI) value was obtained by comparing the weight differences in the samples before and after heating for 60 min at 1,000°C.

RESULTS

Field geology

The metavolcanic rocks of the Godinho antiform are greenish-gray, fine-grained, and present a conspicuous porphyroclastic texture marked by blue quartz porphyroclasts 2–7 mm long (Figure 3A). The main structure observed is a foliation that can be recognized in most of the outcrops described (Figure 3B). Decimeter-long quartz veins with thicknesses varying from 2 to 8 cm occur both parallel and rarely in discordance with the main foliation (Figure 3C). These veins are ideal markers for the reconstruction of the relative sequence of deformation phases. They are deformed into

folded and sigmoid-shaped structures and have a syntectonic origin (Figure 4).

The deformation phase D_1 comprises S_1 , L_1 , and F_1 structures. S_1 is an NW-trending schistosity that also occurs as a mylonitic foliation S_{1m} with moderate to high dip angles toward SW (Figures 5A, 5B, and 6A). The schistosity is marked mainly by the alignment of muscovite and, to a lesser extent, by chlorite, while the mylonitic fabric is characterized mainly by sigma-type porphyroclasts of quartz. L_1 is described as NW-plunging stretching lineation, locally preserved, and restricted to the S_{1m} plane. It is marked by stretched and recrystallized tails of quartz porphyroclasts, sometimes forming millimetric bands (quartz ribbon). Moreover, quartz veins with sigmoidal shapes presenting a top-to-the-SE dextral sense of shear were also observed (Figure 4B). Normally, F_1 presents a complex pattern owing to the overprint of posterior deformational phases. F_1 folds are closed and sometimes isoclinal (Figures 5C and 5D), but in less intensely disturbed parts of the outcrops, they present an axial plane with NNW-trending and plunging hinge lines toward the WNW (Figure 6B). The presence of an axial plane foliation suggests the existence of an earlier fabric, which was not identified on the outcrops and was possibly transposed because of posterior events. Therefore, no evidence was found to distinguish between S_0 and S_{n-1} .

The D_2 phase is represented by S_2 and F_2 structures. S_2 is a well-developed cleavage with NE-trending and moderate to steep dips toward the NW (Figures 5E and 6A). F_2 is represented by centimetric to metric, open to gentle folds,

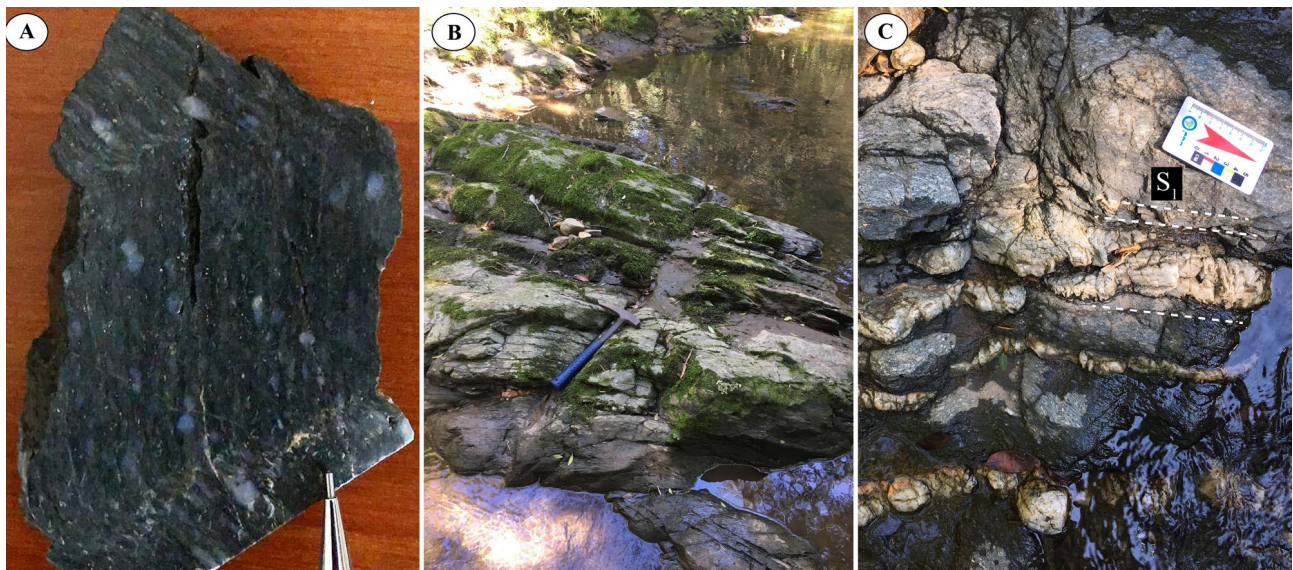


Figure 3. Metavolcanic rocks of the Godinho antiform. (A) Representative sample of the metavolcanic rocks of the Passo da Cuia Region. (B) Representative outcrop located at the Passo da Cuia river. (C) Syntectonic quartz veins sub-parallel to S_1 foliation.



Figure 4. Quartz vein deformed into (A) fold and (B) sigmoid shape.

which are oriented at high angles to F_1 (Figures 5F and 5G). It presents a NE-trending axial plane and a scattered plunge of hinge lines, varying from NNW to WSW (Figure 6B). S_2 is parallel to the axial plane F_2 .

The development of narrow (centimeters to decimeters thick) NNW-SSE semi-ductile shear bands (C_3) occurred in a later-stage D_3 (Figures 5H, 5I, and 6C). In the field, it was possible to observe these shear bands intercepting the S_1 foliation and translating/rotating quartz veins and folds. This structure is responsible for the complex variation of the geometry of folds, which can be related to the different orientations of the fold axis in the shear direction. Folds of all deformation phases are classified as plunging inclined, according to Fleuty (1964).

Petrography

Based on textural criteria, the metavolcanic rocks of the Godinho antiform are classified as schists and mylonites. The identified textures are porphyroclastic, lepidonematoblastic, and mylonitic. The prevailing porphyroclasts are quartz, but orthoclase and plagioclase are also present. These porphyroclasts represent the relics of phenocrysts from the volcanic protolith.

The schistosity is defined by muscovite orientation intercalated with recrystallized quartz (Figure 7A). In mylonitic varieties, porphyroclasts of quartz and feldspar are common (Figure 7B) and found immersed in a fine-grained matrix, with small crystals presenting an average size of 0.025 mm. Locally, these rocks are affected by centimeter shear bands, which can be characterized as an extremely fine matrix with

an average crystal size smaller than 0.025 mm (Figure 7C). Quartz crystals embedded in this fine matrix have 0.30 mm in size and present intragranular fractures. In the shear bands, muscovite crystals are less developed and do not show a preferred orientation. The contact between mylonitic foliation and the millimeter shear bands is abrupt and marked by the decrease in grain size.

Quartz porphyroclasts are anhedral, have an average size of 2.25 mm, and show undulatory extinction. In more deformed samples, they occur either recrystallized or as deformation lamellae and subgrains. The predominant recrystallization mechanism is subgrain rotation recrystallization, generally seen in samples with mylonitic texture (Figure 7B). Bulging recrystallization predominates in the less deformed samples (Figure 7D).

Orthoclase crystals are generally subhedral and vary in size from 1 to 2 mm (Figures 7E and 8A). Plagioclase has an average length of 1.5 mm, presents undulatory extinction, and is almost absent in samples with a high modal concentration of epidote and chlorite. The reason for this decrease in the plagioclase modal might be related to its replacement by these metamorphic minerals (i.e., epidote and chlorite) (Figure 7F).

The matrix of these rocks is mainly composed of recrystallized quartz, muscovite, chlorite, epidote, subordinate amounts of titanite, ilmenite, and rarely small actinolite crystals (Figures 7G, 7H, 7I, 8B, 8C, and 8D). Traces of apatite, pyrite, zircon, and chalcocopyrite are also present. The lepidonematoblastic texture is represented by the alignment of muscovite and sometimes chlorite and actinolite (Figures 7A, 7G, and 7H). Epidotes occur inside plagioclase

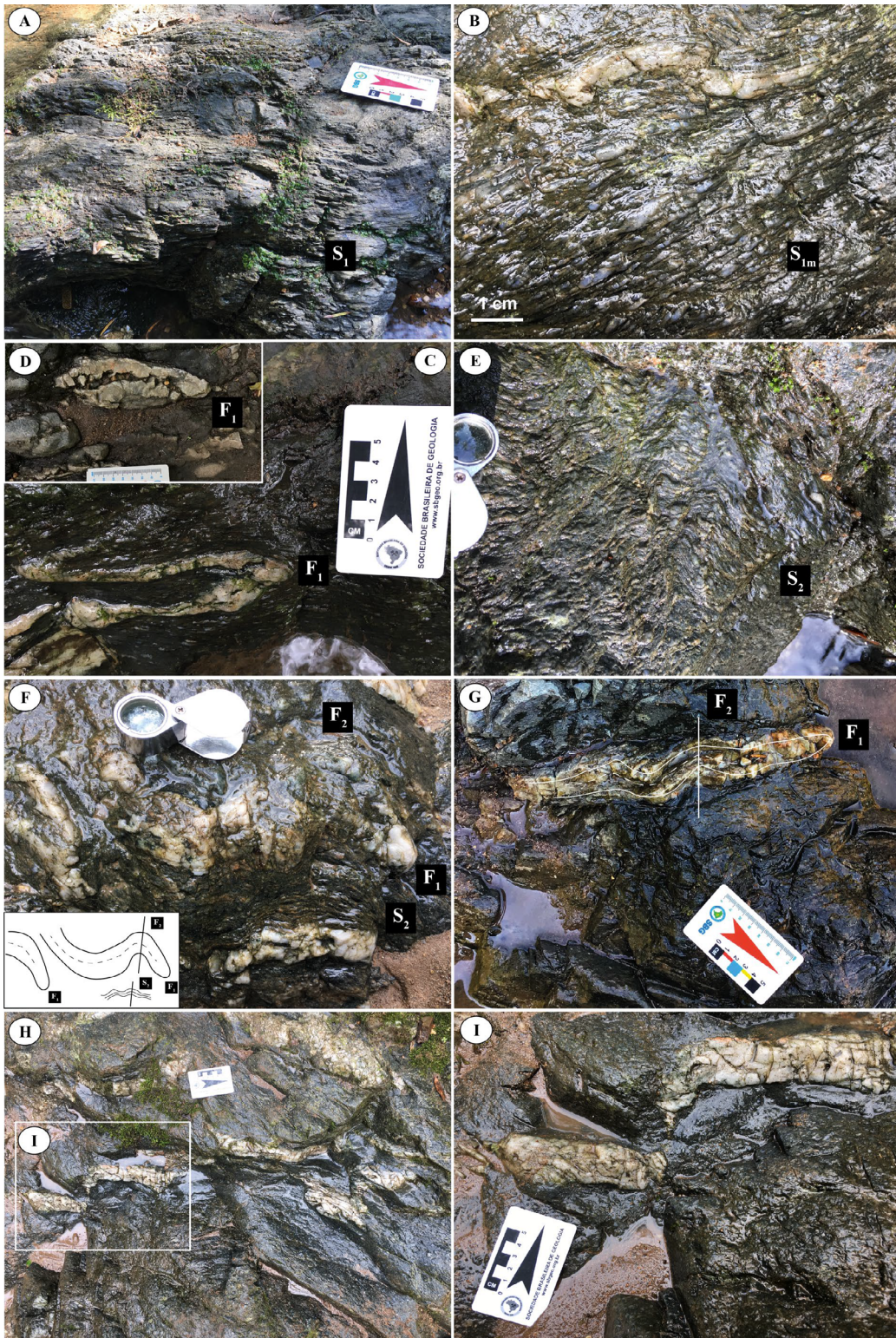


Figure 5. Structural features of the studied metavolcanic rocks. (A) Well-defined schistosity S_1 . (B) S_{1m} mylonitic foliation with stretched quartz porphyroclasts. (C) General features of the closed F_1 fold. (D) Isoclinal F_1 fold. (E) Crenulation cleavage S_2 . (F) Refolding of the F_1 and generation of F_2 folds. (G) F_1 affected by the D_2 . (H) Centimeter-thick shear bands displacing quartz veins. The shear bands do not show abrupt limits, hampering the delimitation of its limits. (I) Quartz vein displacement in detail.

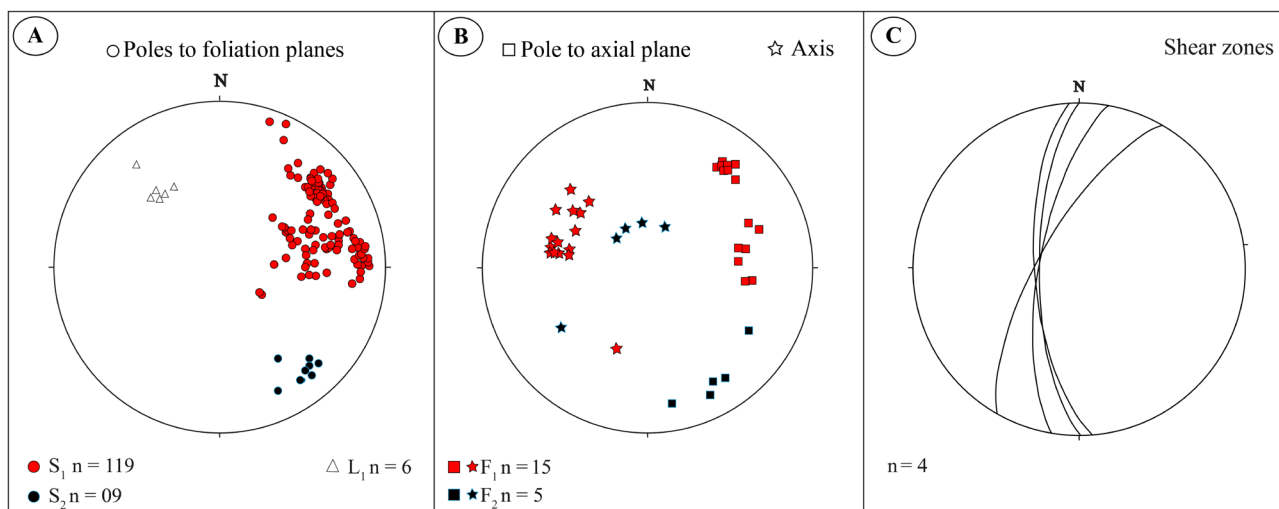


Figure 6. The stereograms are the projection of the lower hemisphere onto the equal area. Planar and linear structures. (A) Poles of S_1 and S_2 foliation planes and L_1 . (B) Poles to axial planes and fold axes of the deformation phases described. (C) Shear bands planes.

crystals or as isolated crystals in the matrix (Figures 7F, and 7I). They consist of euhedral to subhedral crystals with lath shapes and reach 0.25 mm long. Titanites are restricted to the outer border of ilmenite crystals as reaction rims (Figures 7G and 8D). The thickness of the rim is 0.025 mm on average. Sometimes only small relics of ilmenite remain in the newly formed titanite.

Mineral chemistry

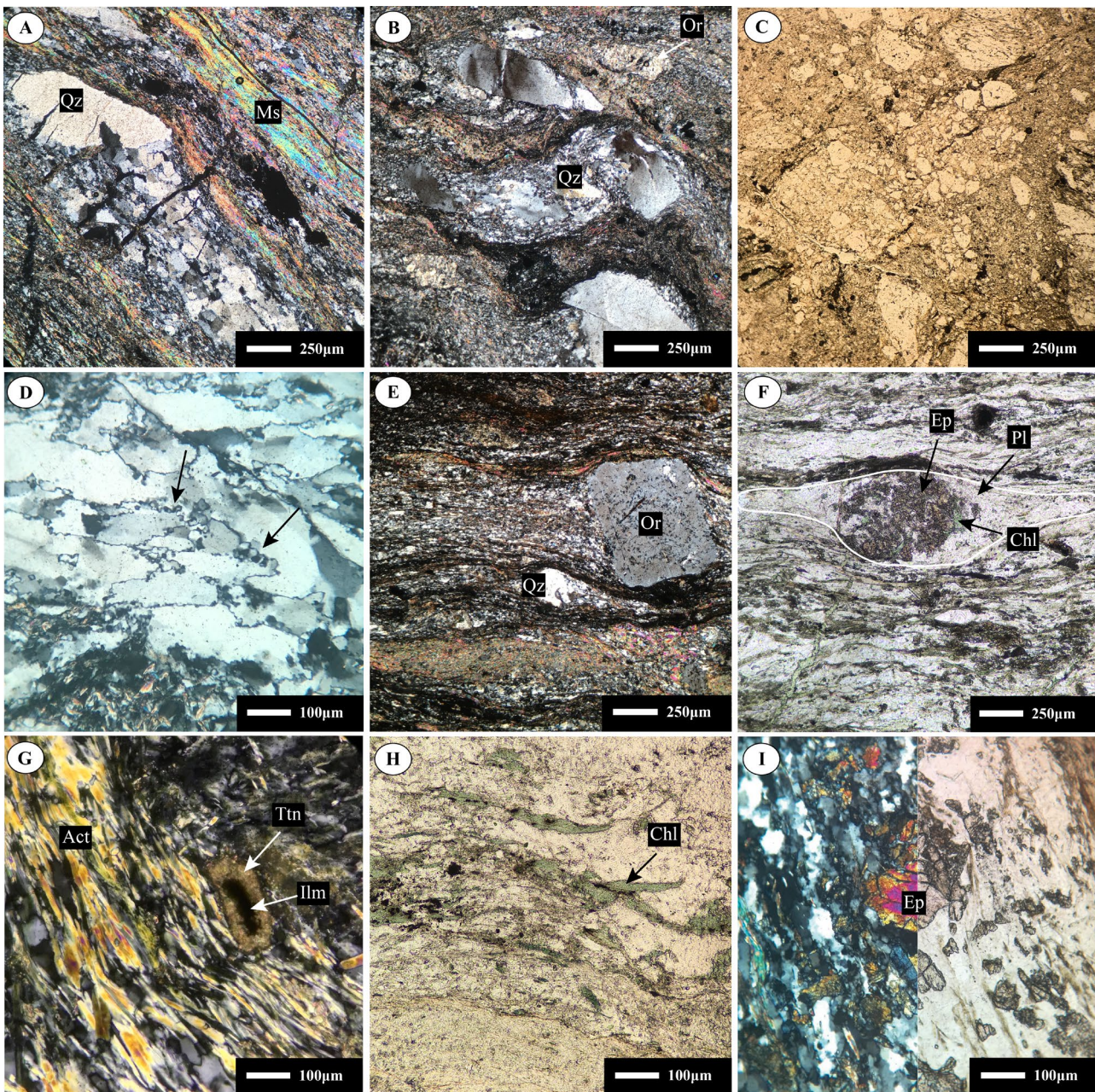
The chemical compositions of selected minerals were determined to classify the relict and metamorphic minerals of the metavolcanic rocks. The analyses were performed on plagioclase, K-feldspar, white mica, chlorite, epidote, titanite, and ilmenite. The average compositions are shown in Table 1.

Plagioclase does not show significant oscillatory zoning. They present a constant albite composition with anorthite end-member nearly absent, with $An_{0.3-0.7}$. On average, the content of orthoclase in the albite crystals is $Or_{0.9}$ with a maximum value of $Or_{3.8}$. In general, orthoclase has albite contents varying between $Ab_{1.5-4.7}$ mol% and anorthite contents reaching a maximum value of $An_{0.4}$. Moreover, one crystal displaying anorthoclase composition ($Ab_{64}Or_{36}$) was also identified (Figure 9A).

For chlorite classification and cation calculation, we use the WinCcac software (Yavuz et al., 2015). The analyzed crystals present Si contents ranging from 2.76 to 3.13 apfu (atoms per formula unit). The X_{Fe} ($Fe/[Fe + Mg]$) values are 0.62 on average. The Al content in the tetrahedral site is 1.08 apfu on average, and in the octahedral site it is 1.21 apfu on average. The Mn content varies from 0.02 to 0.06

apfu. The R^{2+} values vary from 4.68 to 5.05. A variety of diagrams can be used for chlorite classification. The diagram of Moazzen (2004) uses the ratios of $^{IV}Al/(Si + ^{IV}Al)$ and $Fe/(Fe^{2+} + Mg)$ to classify the chlorites. In this diagram, chlorites are mostly plotted in the iron-aluminum clinocllore and magnesium chamosite fields (Figure 9B). In the Zane and Weiss (1998) and Plissart et al. (2009) diagrams, chlorites are classified as belonging to the trioctahedral type (Annex 1). The negative correlation between Fe^{2+} and Mg shown in Figure 9C is due to the substitution of these elements in the cubic sites, which links the chamosite and clinocllore end-members (Deer et al., 2009).

Mica has mostly a phengitic composition with Si/Al ratios in the tetrahedral sites higher than 3.1. The Si contents vary from 3.38 to 3.50 apfu. The total cations, varying from 6.97 to 7.03 apfu, classify these micas as dioctahedral (Baltatzis, 1987). According to Rieder et al. (1998), the phengitic series comprises dioctahedral micas, and they chemically plot between or close to the joins of muscovite-aluminoceladonite and muscovite-celadonite compositional spaces (Tappert et al., 2013). The Si content in the muscovite end-member is between 3.0 and 3.1 apfu (Rieder et al., 1998) while the celadonite end-member shows Si values between 3.5 and 4.0 apfu (Li et al., 1997). Therefore, in this interval is located the phengitic series ($Si = 3.1-3.5$ apfu). The $^{VI}R^{2+}/(^{VI}R^{2+} + ^{VI}R^{3+})$ cationic ratios of these micas are mostly between 0.18 and 0.30 and $Al^{VI}/(Al^{VI} + ^{VI}Fe^{3+})$ between 0.84 and 0.93, corresponding to phengitic series, as shown in Figure 9D by the dashed line (Guidotti and Sassi, 1998). The muscovite and celadonite end-members are linked by the heterovalent Tschermak substitution $Al^{VI}Al^{IV} \leftrightarrow Mg^{VI}Si^{IV}$, as shown in Figures 9E and 9F.

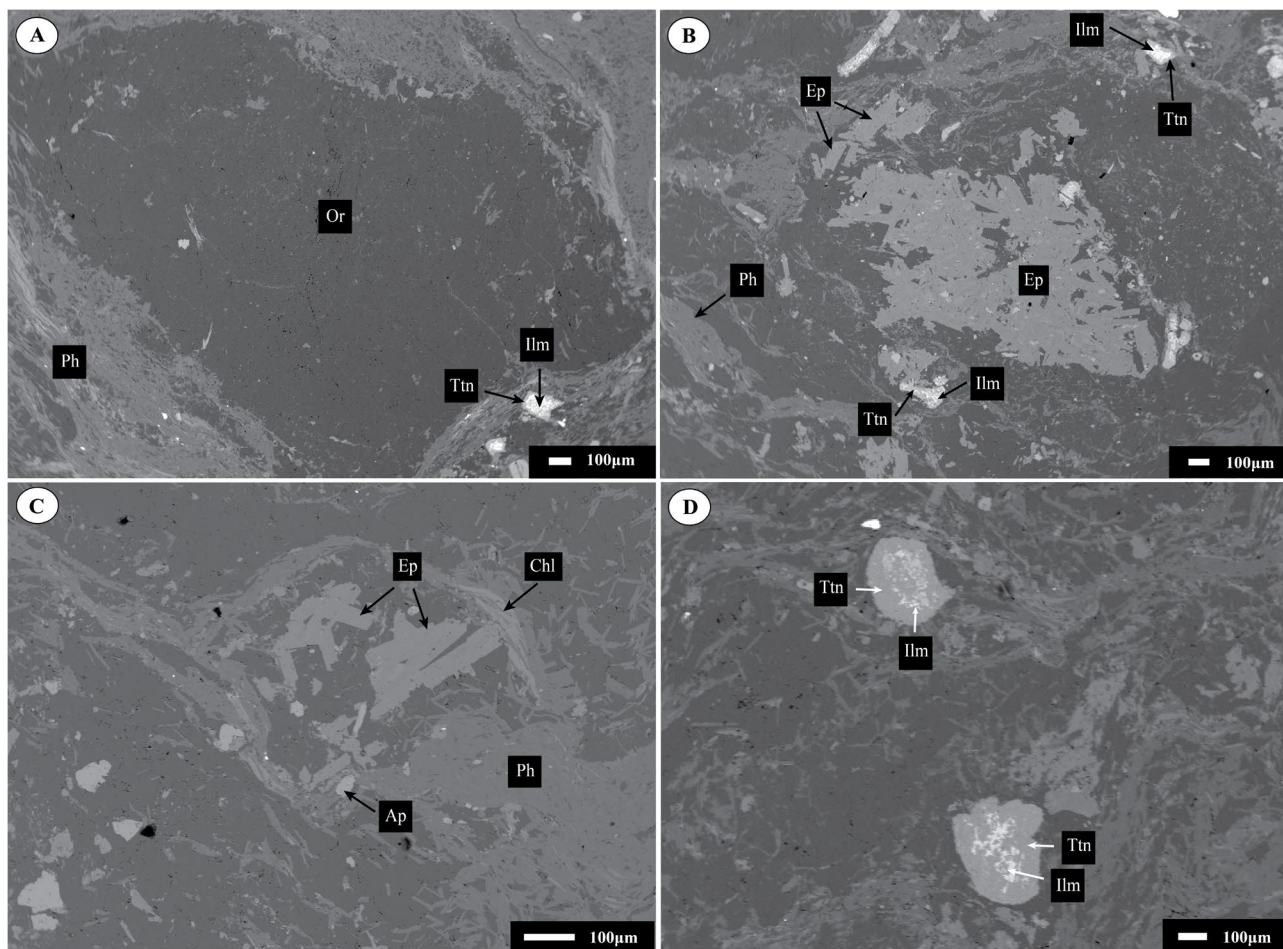


Qz: quartz; Ms: muscovite; Chl: chlorite; Ep: epidote; Act: actinolite; Ttn: titanite; Ilm: ilmenite.

Figure 7. Selected photomicrographs of the studied metavolcanic rocks. (A) Quartz porphyroclast partially recrystallized intercalated with muscovite-rich levels. (B) Quartz porphyroclasts intensely recrystallized. (C) Matrix affected by millimeter shear bands. (D) Bulging recrystallization. Arrows evidencing the characteristic bulges. (E) Euhedral orthopyroxene porphyroclast. (F) Plagioclase porphyroclast replaced by epidote and some chlorite crystals. (G) Actinolite crystals and ilmenite rimmed by titanite. (H) Chlorite crystals oriented in the matrix. (I) Isolated epidote crystals in the matrix.

For epidote classification and cation calculation, we use the WinEpclas software (Yavuz and Yildirim, 2018). The epidote crystals analyzed occur inside plagioclase and also as isolated crystals in the matrix. The Al contents are in the range of 2.01 and 2.46 apfu. The values of Fe^{2+} and

Fe^{3+} are between 0.05–0.41 and 0.19–0.58 apfu, respectively. The Mn (0.00–0.02 apfu), Mg (0.00–0.07 apfu), and Cr (0.00–0.01 apfu) contents are low. These crystals present values of the pistacite component ($\text{Ps} = \text{molar } [\text{Fe}^{3+}/\text{Fe}^{3+} + \text{Al}] \times 100$; Armbruster et al., 2006) between 7 and 19%. The sum of



Qz: quartz; Ph: phengite; Chl: chlorite; Ep: epidote; Ttn: titanite; Ilm: ilmenite.

Figure 8. Back-scatter electron (BSE) images of minerals analyzed at the EPMA. (A) Orthoclase porphyroblast. (B) Subhedral epidote laths and small crystals of ilmenite rimmed by titanite. (C) Association of euhedral epidote associated with phengite, chlorite and apatite. (D) Textural relationships between ilmenite and titanite.

Table 1. EPMA analyses (wt.%) of plagioclase (Pl), orthoclase (Or), mica, epidote (Ept), titanite (Ttn), and ilmenite (Ilm).

	Pl	Anor	Or	Mica	Chl	Ept	Ttn	Ilm
n	17	1	17	30	21	20	16	5
SiO ₂	68.82 (0.97)	66.51	64.64 (0.56)	49.27 (0.96)	26.54 (2.38)	38.70 (0.56)	31.28 (0.77)	0.12 (0.12)
TiO ₂	0.03 (0.04)	0.00	0.02 (0.04)	0.13 (0.25)	0.08 (0.10)	0.09 (0.11)	36.52 (2.54)	51.45 (0.57)
Al ₂ O ₃	18.64 (0.29)	17.69	17.95 (0.23)	24.89 (1.29)	17.71 (1.28)	23.96 (1.85)	1.85 (1.15)	0.02 (0.03)
Cr ₂ O ₃	0.02 (0.03)	0.06	0.03 (0.04)	0.04 (0.04)	0.08 (0.14)	0.06 (0.05)	0.14 (0.12)	0.02 (0.03)
F	n.a.	n.a.	n.a.	n.a.	n.a.	n.a.	0.24 (0.30)	n.a.
FeO	0.25 (0.08)	0.04	0.13 (0.11)	5.11 (1.08)	30.56 (3.14)	8.60 (1.81)	1.05 (0.81)	41.51 (0.95)
MnO	0.02 (0.04)	b.d.	0.03 (0.03)	0.05 (0.04)	0.43 (0.14)	0.16 (0.08)	0.09 (0.10)	5.91 (1.14)
MgO	0.10 (0.02)	0.02	0.01 (0.02)	2.65 (0.50)	10.98 (2.07)	0.14 (0.15)	0.15 (0.29)	0.10 (0.03)
CaO	0.21 (0.18)	0.25	0.03 (0.03)	0.05 (0.19)	0.08 (0.07)	23.13 (0.55)	28.58 (0.64)	0.15 (0.12)
Na ₂ O	10.89 (0.41)	8.41	0.32 (0.10)	0.07 (0.05)	0.07 (0.05)	0.06 (0.09)	0.05 (0.05)	0.03 (0.03)
K ₂ O	0.83 (0.15)	7.03	16.20 (0.27)	10.59 (0.43)	0.46 (1.03)	0.09 (0.19)	0.04 (0.06)	0.01 (0.01)
Cl	0.01 (0.01)	0.00	0.02 (0.02)	0.01 (0.02)	0.02 (0.02)	0.01 (0.01)	0.02 (0.02)	0.01 (0.01)
NiO	0.02 (0.02)	0.04	0.03 (0.03)	0.02 (0.02)	0.02 (0.03)	0.03 (0.03)	0.01 (0.01)	0.01 (0.01)
V ₂ O ₃	0.02 (0.02)	b.d.	0.01 (0.02)	0.03 (0.03)	0.03 (0.02)	0.05 (0.05)	0.74 (0.27)	0.81 (0.07)
Total	99.85	100.05	99.40	92.91	87.06	95.09	100.76	100.15

n: number of analyses; n.a.: not analyzed; b.d.: below detection.

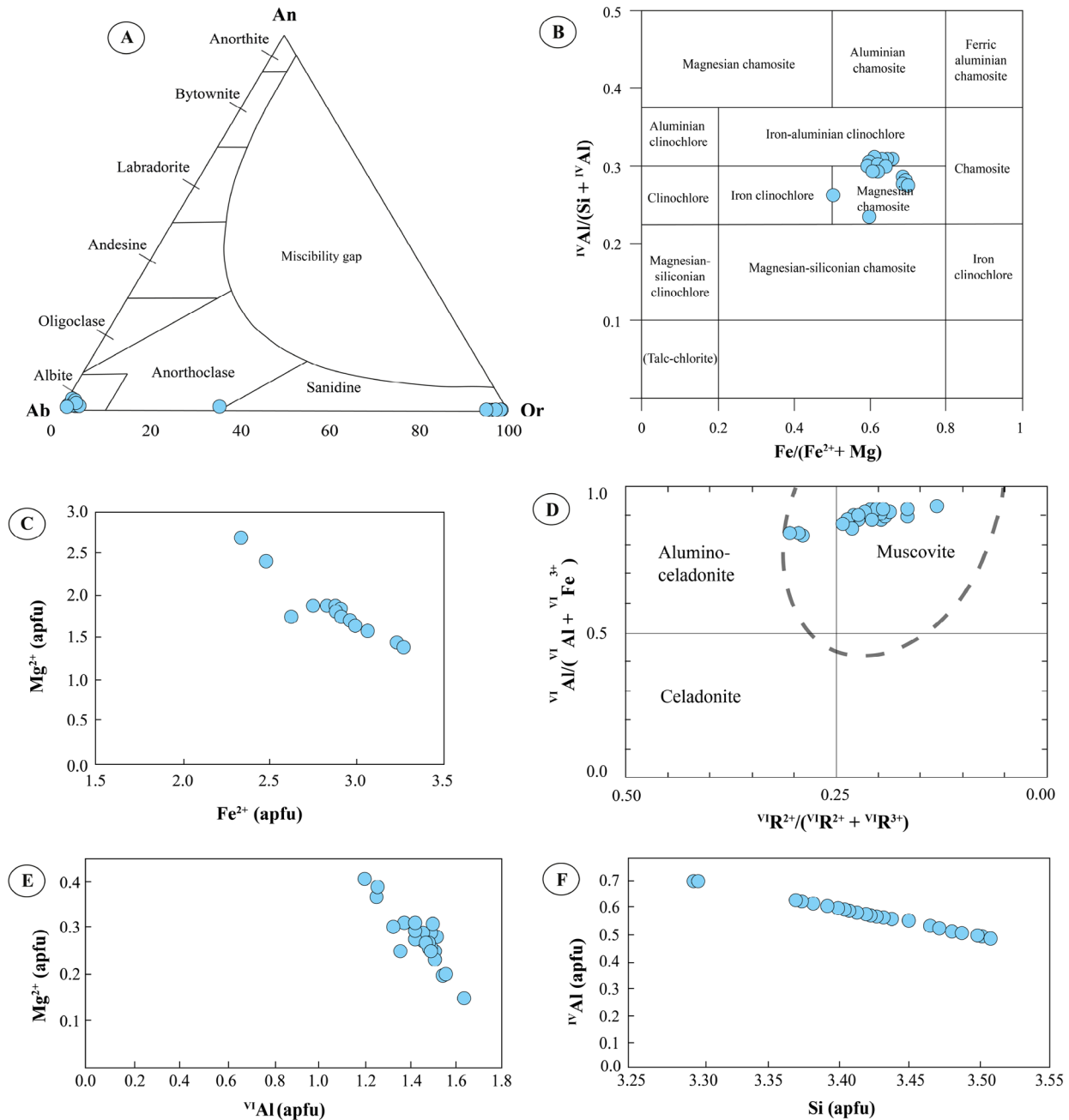


Figure 9. (A) Ab-An-Or ternary plot of feldspar compositions (after Deer et al., 2009). (B) Classification diagram of chlorites in the $^{IV}Al/(Si + ^{IV}Al)$ vs. $Fe/(Fe^{2+} + Mg)$ diagram (after Moazzen, 2004). ^{IV}Al : tetrahedral aluminum. (C) The negative correlation indicates substitution in the chlorite octahedral site. (D) Mica classification diagram (after Guidotti and Sassi, 1998). The phengite compositional range is marked by the dashed line. $^{VI}R^{2+}$: $Mg + Fe^{2+} + Mn$; $^{VI}R^{3+}$: $Al + Fe^{3+}$. $^{VI}Fe^{3+}$: octahedral iron. ^{VI}Al : octahedral aluminum. Fe^{3+} values used in this diagram follow the method proposed by Schmidt et al. (2000) and Auzanneau et al. (2010) for the classification of this specific mineral. (E), (F) The negative correlation between Mg and ^{VI}Al and ^{IV}Al and Si indicates Tschermak substitution.

cations at A-site varies between 1.93 and 2.06 and at M-site between 2.85 and 2.94 apfu. The deficit of the M-site can be related to the typical presence of Sn^{4+} , Nb^{5+} , Cu^{2+} , and Zr^{2+} (Armbruster et al., 2006; Yavuz and Yildirim, 2018).

Titanite occurs always on the outer border of ilmenite crystals. The titanite end-member varies mainly in the interval of 90.17–95.41 mol%. Ilmenite compositions are enriched in the $FeTiO_3$ component (86.00–91.69 mol%) and

also comprise a significant molar proportion of the MnTiO_3 (pyrophanite) component (8.31–14.00 mol%).

Geothermometry

Several studies, based on distinct approaches, have demonstrated the potential of chlorites as a geothermometer (Vidal et al., 2006; Inoue et al., 2010; Trincal et al., 2015; Chinchilla et al., 2016). In this study, empirical to semi-empirical chlorite geothermometers were applied for each electron microprobe analysis. The temperatures obtained can be visualized in Table 2. The geothermometric models of Cathelineau (1988) and Jowett (1991) are based on the Al content presented in the tetrahedral site, whereas the De Caritat et al. (1993) model uses the octahedral vacancy of chlorites to estimate the crystallization temperature. The temperatures obtained using Cathelineau (1988) and Jowett (1991) thermometers present a small average difference of 9°C. The mean temperature acquired by these models is 316°C for Cathelineau (1988) and 325°C for Jowett (1991). The De Caritat et al. (1993) model displays lower temperatures when compared to Cathelineau (1988) and Jowett (1991), with an average of 300°C. The semi-empirical Bourdelle et al. (2013) geothermometer was developed for low-grade metamorphism. The chlorite solid solution of this model involves six end-members (Fe, Mg)-chlorite S,

(Fe, Mg)-sudoite, and (Fe, Mg)-amesite. The calibration of this geothermometer was based on a wide range of chlorite chemical compositions from diverse geological contexts (Bourdelle et al., 2013). This geothermometer provided higher temperatures with an average of 362°C.

Whole-rock geochemistry

The geochemical data of the metavolcanic rocks of the Godinho antiform show small variability in major elements, as observed in Table 3. The alkali content of the samples ($\text{Na}_2\text{O} + \text{K}_2\text{O}$) ranges from 5.11 to 6.08 wt.% and $\text{Na}_2\text{O}/\text{K}_2\text{O}$ ratios are < 1, except for sample PC-23, which shows a slightly higher value (1.03). The Mg# values are in the range of 0.31–0.42. In the classification diagram of Le Bas et al. (1986), the metavolcanic rocks plot in the dacite and rhyolite fields, and based on trace elements (Zr/TiO_2 -Nb/Y; Winchester and Floyd, 1977), they are classified as dacite/rhyodacite (Figure 10B), which suggests that post-magmatic processes did not cause significant chemical changes in the major elements.

Moreover, in the AFM diagram (Irvine and Baragar, 1971), the studied metavolcanic rocks display calc-alkaline character (Figure 10C) and calc-alkaline to high-K calc-alkaline in the Peccerillo and Taylor (1976) diagram (Figure 10D). The values of the alumina saturation index (ASI; molar $\text{Al}_2\text{O}_3/\text{CaO} + \text{Na}_2\text{O} + \text{K}_2\text{O}$) are in the range of 1.01–1.76, which is common for peraluminous composition.

The metavolcanic rocks of the Godinho antiform are enriched in rare-earth elements (REE) ($\Sigma\text{REEs} = 108.32$ – 221.72 ppm) (Table 4). In the chondrite-normalized REE diagram, the metavolcanic rocks demonstrate high REE fractionation ($\text{La}_N/\text{Yb}_N = 7.02$ – 9.65 , where N indicates chondritic normalized values using the data of Boyton, 1984) (Figure 11A). In the primitive mantle-normalized multielement diagram (normalization values from McDonough and Sun, 1995), all samples show the same pattern, characterized by enrichment in large-ion lithophile elements (LILE) (except Sr) and strong negative anomalies of high field strength elements (HFSE) (Nb, Ta, and Ti) (Figure 7D).

Within the ternary Rb-Hf-Ta diagram of Harris et al. (1986) (Figure 12A) and in the Rb-Y+Nb diagram of Pearce et al. (1984) (Figure 12B), the samples are plotted in the volcanic arc field. Similarly, in the La/10-Y/15-Nb/8 plot of Cabanis and Lecolle (1989), the samples also occupy the active margins field (Figure 12C). The Nb/Yb-Th/Yb diagram of Condie and Kröner (2013) can clearly distinguish between MORB-OIB mantle array from arc setting and also island arc from continental arc. The metavolcanic rocks have Th/Yb (3.7–6.5) and Nb/Yb (3.0–5.4) ratios typical of continental arc fields (Figure 12D). In the $(\text{La}/\text{Yb})_N$ and Sr/Y diagram proposed by the same authors, the studied samples plotted close to the continental arc field (Figure 12E) and

Table 2. Temperatures obtained by the empirical to semi-empirical models (°C).

Cathelineau (1988)	Jowett (1991)	De Caritat et al. (1993)	Bourdelle et al. (2013)
313	322	302	
274	280	298	
**		304	367*
333	342	320	
336	345	329	
326	335	308	429*
322	331	292	359*
314	323	285	334
327	336	305	373*
331	341	304	401*
336	347	309	
334	344	306	
323	331	306	383*
288	300	279	316
297	309	288	335
293	304	278	317
305	316	289	373*
316	325	300	362

*Temperatures above the limit of applicability; **chlorite compositions that do not satisfy model's criteria were not included. Bold numbers represent average temperatures.

Table 3. Whole-rock major element compositions (wt.%) of the metavolcanic rocks of the Godinho antiform.

Sample	PC-01	PC-07	PC-19	PC-20	PC-22	PC-23	PC-24	PC-25	PC-26
SiO ₂	68.59	71.45	68.5	67.82	69.42	71.98	71.37	66.51	63.14
TiO ₂	0.68	0.46	0.65	0.68	0.46	0.48	0.46	0.68	0.79
Al ₂ O ₃	13.72	13.49	13.83	14.05	13.94	13.55	13.91	13.85	15.43
FeO	5.84	4.66	5.37	5.57	5.04	4.35	4.25	4.84	6.41
MnO	0.07	0.05	0.07	0.07	0.13	0.05	0.04	0.06	0.08
MgO	2.43	1.34	1.86	1.95	1.33	1.23	1.28	1.74	2.31
CaO	0.66	0.42	0.85	1.40	0.70	0.22	0.20	3.10	2.01
Na ₂ O	1.99	2.70	2.04	2.15	2.87	2.96	2.72	2.84	2.77
K ₂ O	3.12	2.84	3.61	3.30	3.13	2.86	3.36	3.11	3.8
P ₂ O ₅	0.11	0.08	0.12	0.13	0.09	0.08	0.09	0.16	0.20
Cr ₂ O ₃	0.007	0.004	0.006	0.006	0.004	0.003	0.003	0.007	0.01
LOI	2.60	2.40	2.90	2.70	2.70	2.10	2.20	2.90	2.80
Total	99.87	99.91	99.86	99.87	99.89	99.92	99.90	99.86	99.84

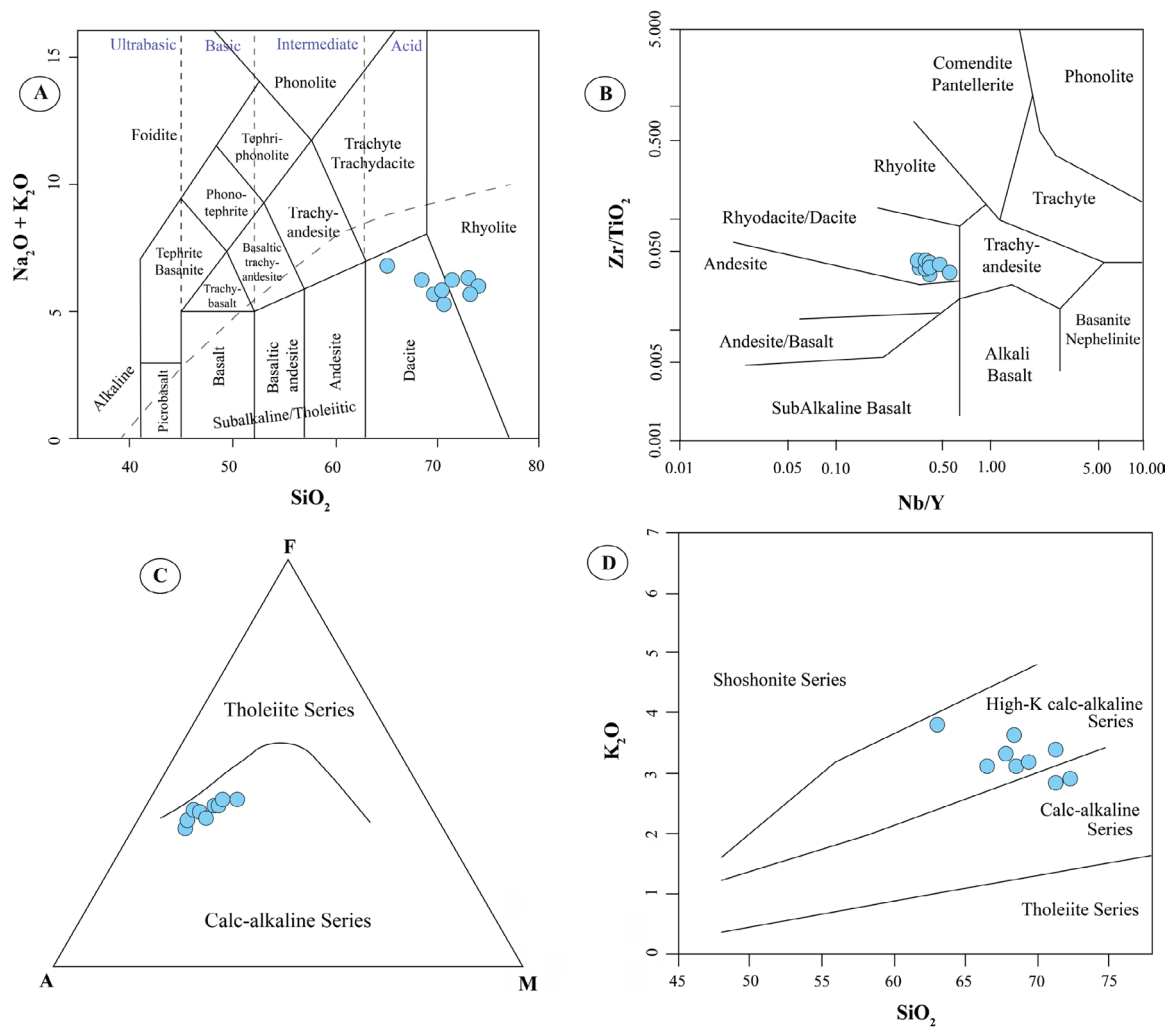
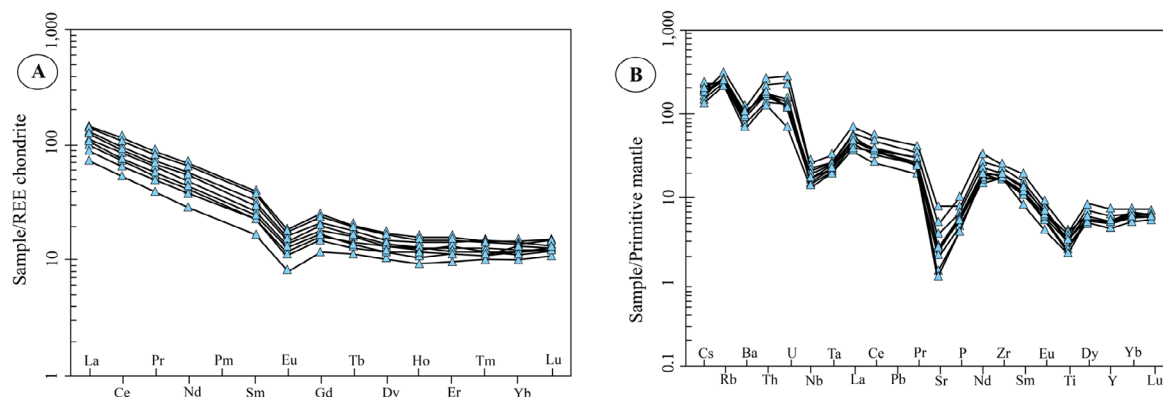
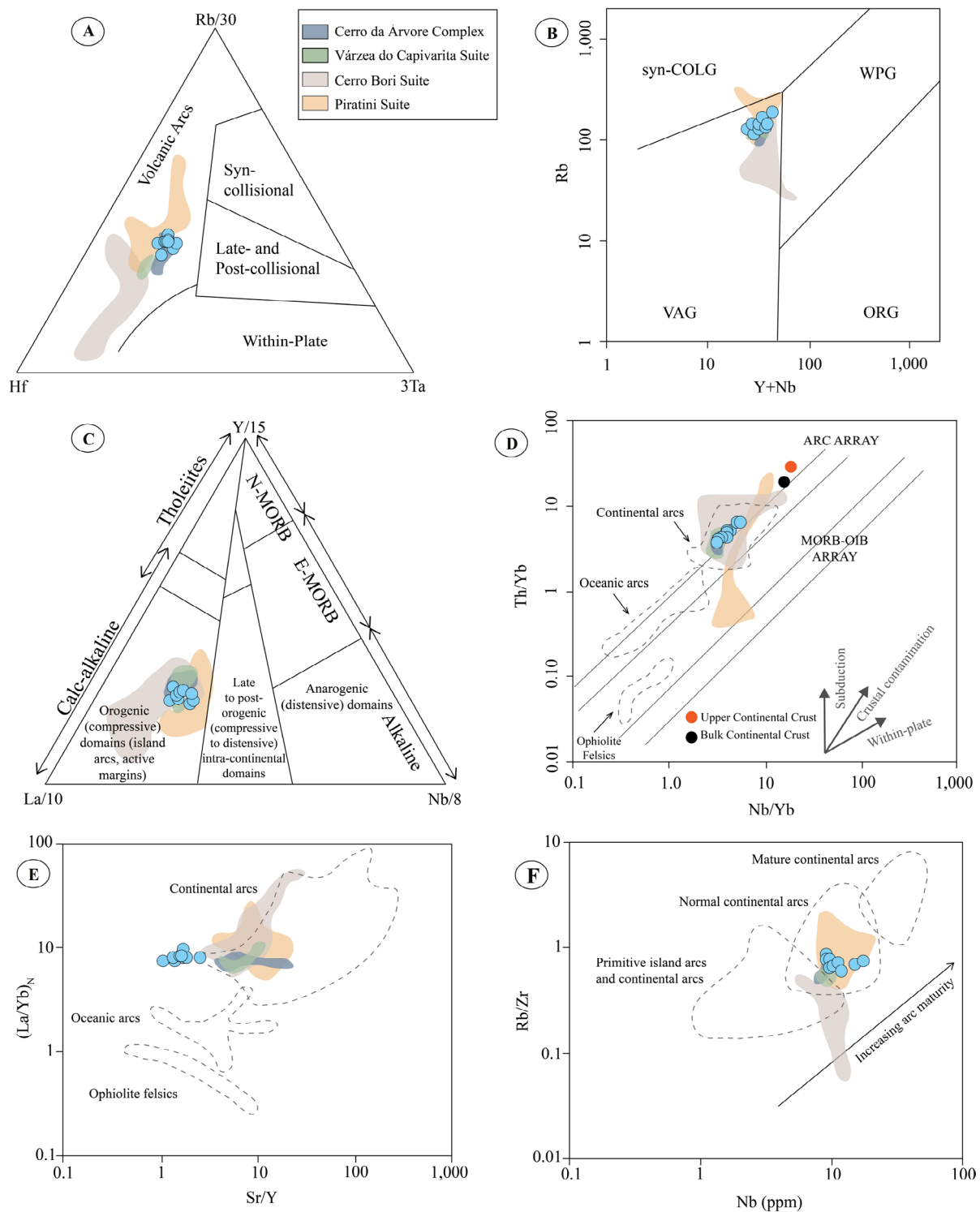

Figure 10. Whole-rock geochemical characteristics of major and trace elements of the metavolcanic rocks from Godinho antiform. (A) $\text{Na}_2\text{O} + \text{K}_2\text{O}$ (wt.%) versus SiO_2 plot (TAS) (after Le Bas et al., 1986). (B) Zr/TiO_2 versus Nb/Y plot (after Winchester and Floyd, 1977). (C) AFM diagram (after Irvine and Baragar, 1971). (D) SiO_2 versus K_2O plot (after Peccerillo and Taylor, 1976).

Table 4. Whole-rock trace element compositions (ppm) of the metavolcanic rocks of the Godinho antiform.

Sample	PC-01	PC-07	PC-19	PC-20	PC-22	PC-23	PC-24	PC-25	PC-26
Ni	< 20	< 20	< 20	< 20	< 20	< 20	< 20	< 20	< 20
Sc	16.00	13.00	14.00	15.00	12.00	12.00	13.00	15.00	18.00
V	94.00	59.00	81.00	82.00	58.00	57.00	54.00	88.00	102.00
Sn	2.00	3.00	3.00	3.00	2.00	2.00	2.00	4.00	4.00
W	1.10	1.30	1.00	1.50	1.10	0.90	0.70	1.10	1.40
Cs	4.90	3.30	3.10	3.20	4.60	2.70	2.90	2.80	3.90
Ba	494.00	465.00	621.00	625.00	457.00	452.00	495.00	638.00	772.00
Be	1.00	6.00	3.00	4.00	1.00	1.00	1.00	4.00	2.00
Co	15.90	9.50	13.50	12.80	7.70	8.20	7.80	11.60	14.00
Rb	139.30	127.60	168.80	142.00	153.20	129.90	149.10	152.40	188.70
Sr	39.60	27.30	43.20	71.50	50.60	24.80	23.00	156.70	96.70
Hf	5.70	4.70	6.40	6.50	5.40	5.00	5.40	5.90	6.80
Zr	208.30	167.30	238.80	236.90	183.90	174.40	190.70	212.10	248.70
Y	24.20	20.90	26.30	27.50	26.60	18.50	21.80	26.80	30.90
Ta	0.70	0.70	0.90	0.90	0.80	0.70	0.80	1.00	1.20
Nb	10.20	9.00	11.00	11.40	9.10	8.90	9.00	14.80	17.00
Ga	15.20	14.70	15.90	16.00	14.80	13.70	14.00	14.80	15.40
Th	11.20	10.70	13.40	14.10	11.10	10.40	11.10	17.60	20.90
U	2.50	2.40	2.70	3.00	2.60	1.40	2.40	4.80	5.60
La	31.70	29.50	40.80	35.10	34.00	23.70	29.90	37.50	45.00
Ce	61.70	57.30	78.90	68.10	66.90	44.30	60.30	77.90	93.20
Pr	6.91	6.51	9.05	7.84	7.50	4.98	6.78	9.04	10.71
Nd	25.70	24.40	33.90	29.30	28.70	18.40	25.80	35.10	42.00
Sm	4.76	4.63	6.38	5.36	5.22	3.39	4.76	6.55	7.86
Eu	0.93	0.84	1.19	0.97	1.02	0.62	0.84	1.16	1.32
Gd	4.44	4.15	5.33	4.86	4.89	3.15	4.22	5.55	6.50
Tb	0.71	0.65	0.82	0.81	0.77	0.55	0.71	0.86	0.96
Dy	4.25	3.93	4.65	4.83	4.74	3.42	4.34	4.67	5.56
Ho	0.91	0.78	0.94	1.00	1.01	0.70	0.92	1.01	1.12
Er	2.77	2.49	2.72	2.95	2.89	2.13	2.86	2.92	3.31
Tm	0.40	0.38	0.41	0.47	0.47	0.34	0.41	0.41	0.48
Yb	2.63	2.52	2.85	3.03	2.99	2.27	2.87	2.72	3.22
Lu	0.41	0.41	0.43	0.50	0.43	0.37	0.43	0.41	0.48
ΣREE	148.22	138.49	188.37	165.12	161.53	108.32	145.14	185.80	221.72
(La/Sm) _N	4.90	4.01	4.02	4.12	4.10	4.40	3.95	3.60	3.60
(Gd/Yb) _N	1.38	1.32	1.50	1.29	1.31	1.11	1.18	1.64	1.62
(La/Yb) _N	8.13	7.89	9.65	7.81	7.67	7.04	7.02	9.29	9.42
Ce _N	76.36	70.92	97.65	84.28	82.80	54.83	74.63	96.41	115.35
Sm/Yb	1.80	1.83	2.23	1.76	1.74	1.49	1.65	2.40	2.44
Sr/Y	1.63	1.30	1.64	2.60	1.90	1.34	1.05	5.84	3.12
Eu/Eu*	0.62	0.59	0.62	0.58	0.62	0.58	0.57	0.59	0.56

**Figure 11.** (A) Chondrite-normalized REE patterns. Normalization values were obtained from Boyton (1984). (B) Primitive mantle-normalized multielement diagrams. Normalization values were obtained from McDonough and Sun (1995).



Syn-COLG: syn-collision granites; VAG: volcanic arc granites; WPG: within plate granites; ORG: ocean ridge granites.

Figure 12. Trace element discriminant diagrams used for geological setting classification of the metavolcanic rocks of the Godinho antiform and correlated units. The geochemistry of the compared rocks will be discussed in a separated section. (A) Hf-Ta-Rb ternary diagram (after Harris et al., 1986). (B) Y+Nb-Rb diagram (after Pearce et al., 1984). (C) La-Nb-Y ternary diagram (after Cabanis and Lecolle, 1989). (D) Th/Yb-Nb/Yb diagram (after Condie and Kröner, 2013 modified from Pearce, 2008). Continental crust averages are from Rudnick and Gao (2003). (E) Sr/Y-(La/Yb)_N diagram (after Condie and Kröner, 2013). (F) Nb-Rb/Zr diagram (after Brown et al., 1984).

considerably far from the island arc field, which is related to $(La/Yb)_N$ ratios commonly higher in continental arc rocks than in island arc rocks. Moreover, in all diagrams of Schandl and Gorton (2002), specially created to classify intermediate to felsic rocks, even those affected by metamorphism and hydrothermal alteration, the metavolcanic samples of the Godinho antiform plotted are within the active continental field (Annex 2). To assess the maturity of the continental arc, the Rb/Zr-Nb diagram of Brown et al. (1984) was applied, which is divided into primitive, normal, and mature island arcs and continental arcs (Figure 12F). In this diagram, the metavolcanic rocks of the Godinho antiform occupy the normal continental arc field.

DISCUSSION

Structures and metamorphism

The studied area does not present previous in-depth studies focused on the structural evolution of the Godinho antiform. Nevertheless, it is still interesting to develop reasoning regarding the comparison of similar aspects of deformation/rheological mechanisms described in studies that were carried out in the Porongos Complex. It should be emphasized that this comparison does not concern temporal correlations.

D_1 presents the most penetrative structures, with the prevalence of simple shear. S_1 is a well-developed NW-trending schistosity that progresses to a mylonitic foliation. The mylonitic foliation presents σ -type porphyroclasts and quartz veins, indicating dextral shear sense. F_1 are centimetric to decimetric closed to isoclinal folds parallel to S_1 . Vergence of these folds is toward ENE, and a stretching L_1 occurs parallel to the F_1 axis. The stretching occurs along both the x and y axes of the finite deformation ellipsoid, which is characterized as a transpressive deformation. The presence of an axial plane foliation suggests the existence of an earlier fabric, yet no evidence was found to distinguish between an S_0 or S_{n-1} . Battisti et al. (2018) reported that the main layering was not found, and Saalman et al. (2006) affirmed that it is not, indeed, observable in the metavolcanic rocks of PC. Therefore, in the present study, as described by Battisti et al. (2018), D_1 is equivalent to D_2 described by Saalman et al. (2006). D_2 is a semi-ductile stage characterized by a well-developed NE-trending S_2 cleavage and centimetric to metric, open to gentle F_2 folds. They occur parallel to S_2 and present vergence toward SE.

In fold and thrust belts, stresses are relieved mainly through regional shear zones. In this context, the high angle between the shear bands described in D_3 and the D_2 structures suggests that they could act like stress dissipation surfaces in the semi-ductile stages. These shear bands are narrow and trend toward NNW.

More recently, Battisti et al. (2018) highlighted that the PC rocks may register two thrusting episodes, one during peak metamorphic conditions and another under retrograde metamorphic conditions, which could be compatible with one main progressive event herein described as D_1 and the other in D_2 . In this study, the vergence of folds is toward NE in D_1 while SE in D_2 .

The metamorphic conditions in the Porongos Complex have been addressed by some authors as varying from greenschist to amphibolite facies. The peak PT conditions were established between 550 and 580°C and 4.5 and 6.3 kbar at 662–563 Ma (Lenz, 2006; De Toni et al., 2021; Battisti, 2022). In the Godinho antiform, the greenschist facies assemblage is widespread in the metavolcanic rocks and is represented by phengite + chlorite + clinozoisite-epidote + albite + quartz \pm actinolite. This metamorphism has had a pervasive character and is widespread in the rocks of the studied area.

According to Pearce and Wheeler (2014), the anorthite component of plagioclase can react with biotite to form chlorite and epidote, which might explain the relicts of plagioclase crystals substituted by epidote and chlorite. Phengitic mica is present in a variety of metamorphic rocks. The cationic ratios obtained for this mineral are comparable with those obtained from greenschist facies (Wise and Eugster, 1964). The excess in the octahedral sites ($\Sigma VI > 2$) of the phengitic mica was suggested by Guidotti (1984) as a slight deviation from dioctahedral to trioctahedral composition and associated with a metamorphic function.

The chlorite crystallization temperatures of the metavolcanic rocks of the Godinho antiform indicate greenschist facies, considering the models applied. The model of Cathelineau (1988) can be used for a wide range of rock types, presents a great regressive coefficient [$Al^{IV-T}(^{\circ}C)$, $r = 0.97$], and has a small difference in temperatures relative to the other empiric models. The semi-empiric model of Bourdelle et al. (2013) was created for low-grade metamorphism and is characterized as a new pure- Fe^{2+} thermometer. The large dataset involved in the semi-empiric model of Bourdelle et al. (2013) compensates for the non-ideality and Fe^{3+} issues of an application of chlorite geothermometer. However, it is noteworthy that this semi-empiric method is reliable only for temperatures $< 350^{\circ}C$, which in this case does not fit with the studied samples since some chlorite compositions of the metavolcanic rocks of the Godinho antiform display temperatures above the limit of applicability. Moreover, some chlorite compositions are not suitable for this model (Bourdelle et al., 2013) and were not included in this study (Table 2). Therefore, although the semi-empiric model of Bourdelle et al. (2013) is a more robust method compared to the empiric ones, it does not apply to most of the chlorite compositions of the metavolcanic rocks of the Godinho antiform. Thus, the temperatures obtained using the Cathelineau (1988) geothermometer are best suited

to represent the temperature of greenschist facies of these metavolcanic rocks (316°C). The quartz recrystallization mechanism (subgrain rotation and bulging recrystallization) associated with incipient feldspar recrystallization reinforces the greenschist facies conditions imprinted in these rocks (Passchier and Trouw, 2005).

Tectonic setting

The felsic calc-alkaline peraluminous metavolcanic rocks of the Godinho antiform are essentially enriched in LILE and light rare-earth elements (LREE) and depleted in HFSE (Figure 11). The multielement diagram shows negative Nb, Sr, P, Ti, and Ta anomalies, which resemble those characteristics of magmatic arcs (Wilson, 1989; Hawkesworth et al., 1993; Stern, 2002; Gill, 2010; Condie and Kröner, 2013). Moreover, the enrichment in LILE and LREE is due to the addition of a subducted-related component (Hawkesworth et al., 1993; Stern, 2002). The different behavior of LILE, as they are more mobile and soluble elements relative to HFSE, is associated with the contrasting partition coefficient of these elements into a fluid-rich phase (Brenan et al., 1995). On the contrary, the depletion in Nb and Ta is still disputable; nevertheless, some studies point out the presence of residual HFSE-rich minerals (Ti-bearing minerals) in the magma source (Ionov et al., 1999; Kendrick and Yakymchuk, 2020), crustal contamination (Jahn et al., 1999), or several stages of partial melting followed by melt extraction in the source (Gill, 2010).

To confirm that the magmas responsible for forming the studied metavolcanic rocks originated in a volcanic arc as the main tectonic setting, trace element diagrams were used, which are useful tools for identifying geotectonic environments. In the Harris et al. (1986) diagram, the studied metavolcanic rocks plot in the group I field (Figure 12A). According to these authors, the group I field (volcanic arc) in their diagram represents magmas that were modified by a subducted-related component and are enriched in LILE. The discrimination diagram of Pearce et al. (1984) (Figure 12B), designed to classify granite-type rocks, can also be used for classifying volcanic rocks, as the Rb-(Y+Nb) concentration strongly reflects the source of magmas (Pearce, 1996). The diagnostic features of volcanic arc rocks in this diagram are mainly the low content of (Nb+Y) and also the high content of Rb (Pearce, 1996). In this diagram, the studied rocks also plot in the volcanic arc field.

The Th enrichment in arc magmas relative to other tectonic settings is associated with the sediment contribution from the downgoing slab (Hawkesworth et al., 1997) since its solubility in the subducted fluid has been shown to be extremely low (Bailey and Ragnarsdottir, 1994). In contrast, Ta contents are not modified by the subduction processes and then remain constant. Thus, in a within-plate setting, the

Th and Ta contents are roughly equal (Brown et al., 1984). Gorton and Schandl (2000) proposed that intermediate to felsic rocks formed in the within-plate setting have the lowest Th/Ta ratios (1–6), active continental margin rocks have intermediate values (6–20), and the highest values can be found in island arc rocks (20–90). The studied samples have Th/Ta ratios between 13.8 and 17.6, in agreement with an active continental arc environment (Gorton and Schandl, 2000).

The above-applied tectonic discriminant diagram (Pearce et al., 1984; Harris et al., 1986) (Figures 12A and 12B) was not designed to distinguish between continental arc and island arc settings; therefore, other diagrams must be applied. The increasing ratios of Nb/Yb, Th/Yb, La/Yb_N, and Sr/Y in the Condie and Kröner (2013) diagrams (Figures 12D and 12E) normally reflect differentiation processes since Nb, Th, La, and Sr are more incompatible than Yb and Y (Pearce, 2008). In these diagrams, the metavolcanic rocks also plot in the field of the continental arc.

Additionally, these metavolcanic rocks plot in the normal continental arc field in the Brown et al. (1984) diagram and are considerably far from the primitive continental arc field (Figure 12F), suggesting that during the formation of the volcanic rocks of the Godinho antiform, the arc was relatively mature. Considering the remarkable geochemical signatures of subducted-related magmas in the studied metavolcanic rocks, a continental arc setting was responsible for the generation of the metavolcanic rocks of the Godinho antiform from the Porongos Complex.

Previous geochemical data of continental arc rocks

A continental arc environment with Tonian age was proposed for the origin of the Cerro Bori orthogneiss (CB; Lenz et al., 2013), Piratini Suite (PS; Tambara, 2015), Várzea do Capivarita orthogneiss (VC; Martil et al., 2017), and the metavolcanic rocks of the Cerro da Árvore Complex (CA; Battisti et al., 2018) in the PC, all located in the DFB. These rocks share many geochemical features with the metavolcanic rocks studied here. Most samples plot within the calc-alkaline field, except for one sample (CB) that plots within the tholeiitic field (Irvine and Baragar, 1971). Using trace element ratios (Nb/Y-Zr/Ti) for protolith characterization, it is observed that a continuous spectrum from trachy-andesite to dacite-rhyolite was formed. The REE contents of CA ($\Sigma\text{REE} = 136.12\text{--}172.19$ ppm) and VC ($\Sigma\text{REE} = 129.31\text{--}145.64$ ppm) are similar to those obtained for the studied metavolcanic rocks; CB ($\Sigma\text{REE} = 131.42\text{--}387.17$ ppm) and PS ($\Sigma\text{REE} = 86.5\text{--}301.47$ ppm) present some higher values. When normalized by chondritic values (Boyton, 1984), all samples are enriched in LREE relative to heavy rare-earth elements (HREE), with HREE presenting a flat pattern

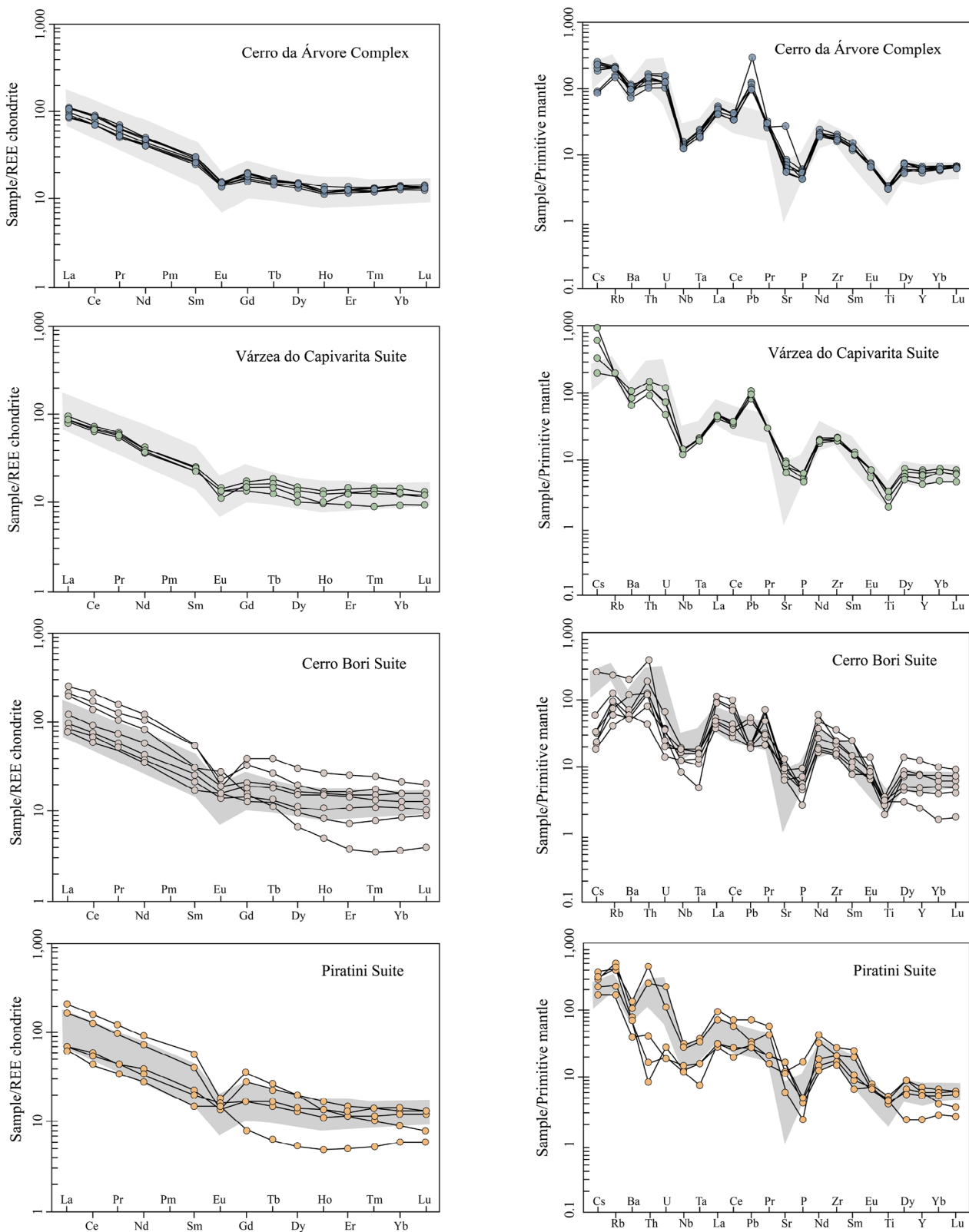


Figure 13. Chondrite-normalized REE patterns and primitive mantle-normalized multi-element spider diagrams of the rocks compared. Gray fields represent the patterns of the metavolcanic rocks from the Godinho antiform of this study. Chondrite and primitive mantle normalization values after Boyton (1984) and McDonough and Sun (1995), respectively.

(Figure 13). Trace elements normalized by primitive mantle (McDonough and Sun, 1995) of all samples compared here are enriched in LILE relative to HFSE with negative Nb, Ta, Sr, P, and Ti anomalies, strongly similar to the studied metavolcanic rocks of the Godinho antiform (Figure 13), suggesting a subducted related origin for these rocks of the central and eastern domains of DFB. According to Coira et al. (1993), La/Ta ratios > 40 and Ba/Ta > 800 are typical signatures of rocks formed in arc sources, while La/Ta ratios < 10 and Ba/Ta < 100 are characteristic of rocks generated in intraplate settings. The range of these ratios for the metavolcanic rocks of the Godinho antiform and the rocks they are being compared to is most in accordance with arc settings (La/Ta = 32–117; Ba/Ta = 545–4616).

This assumption is further straightened by the trace element discriminant diagram. In Harris et al.'s (1986) tectonic diagram, the samples are classified as belonging to the volcanic arc field (Figure 12A). Similarly, in the Pearce et al. (1984) diagram (Figure 12B), samples are plotted in the volcanic arc granite field with the metavolcanic rocks studied here presenting a trend toward within-plate setting. According to Wilson (1989), this trend associated with high K_2O contents might reflect an increase in arc maturity, which might be assumed here. Moreover, in the diagram of Cabanis and Lecolle (1989), all samples were plotted in the active margins field (Figure 12C). The vertical trending observed in Harris et al. (1986) and Cabanis and Lecolle (1989) diagrams toward the apex might be related to a larger interaction with crustal sources, as pointed out by Vieira et al. (2019). Furthermore, in the Th/Yb-Nb/Yb and $(La/Yb)_N$ -Sr/Y diagrams of Condie and Kröner (2013), the compared rocks plot in the field of the continental arc (Figures 12D and 12E), and the vertical trending observed in the Th/Yb-Nb/Yb diagram reflects a subducted-related component input due to an increase in Th/Yb ratios.

An interesting issue demonstrated by these geochemical data is the low involvement with mantle sources. It is widely accepted that the geochemical features of magmas in subduction zones change from the pre-collisional stages to the late- to post-collisional stages, due to the subduction component input in the former stages and slab break-off and lithosphere delamination in the latter stages. However, the variation in the geochemical pattern is fairly limited between the rocks compared, as can be seen in the multielement diagrams (Figure 13).

In summary, the geochemical features of the studied metavolcanic rocks from the Godinho antiform are in great accordance with the metavolcanic rocks from the northern region (Cerro da Árvore Complex) of the PC, Várzea do Capivarita, Cerro Bori, and Piratini orthogneisses. Therefore, we suggest that these units and the metavolcanic rocks from the Godinho antiform represent a relic assemblage formed in an arc setting during the Tonian.

Tectonic implications

Several tectonic models were proposed for the Tonian tectonic evolution of the DFB. The number of orogenies is not consensual and varies according to the proposed model with distinct combinations of Passinho, São Gabriel, Dom Feliciano, and Piratini events. The São Gabriel terrane records the early Brasiliano orogenic events in the DFB, including oceanic crust formation since 920 Ma followed by westward subduction in an intra-oceanic arc between 767 and 757 Ma (Cerva-Alves et al., 2020). An alternative model considers that the São Gabriel terrane records the early stages of a single arc development with an evolution between 925 and 700 Ma. This arc would comprise a more evolved magma reservoir, which could include other tonian relicts of the DFB such as the Porto Belo Complex (Santa Catarina State), the Várzea do Capivarita Complex, and the Cerro do Bori (Uruguay) (De Toni et al., 2020). De Toni et al. (2020) argued that variations in the subduction angle would explain the evolution from fore-arc to back-arc rift setting during the Tonian time. However, the positive isotopic signature of the São Gabriel terrane evidences the juvenile nature of the magmatism with 1.1 Ga T_{DM} (Saalman et al., 2005; Lena et al., 2014; Cerva-Alves et al., 2020), quite different from the other relicts that present highly evolved signatures and 1.7 to 2.2 Ga T_{DM} (Saalman et al., 2006; Martil et al., 2017; Pertille et al., 2017). Therefore, we considered that there were at least two arcs in the Tonian frame of the southern DFB. The second arc that could have formed in this region would be the Piratini arc, recently revised by Vieira et al. (2019). According to Vieira et al. (2019), the Piratini arc would have been formed due to the eastward subduction of the Charrua Ocean beneath a Paleoproterozoic crust between 800 and 680 Ma. Recently, Battisti et al. (2023) proposed an active continental margin (Andean-type) for the origin of the Tonian magmatism in the Várzea do Capivarita and Porongos Complex. According to the authors, the Porongos Complex (Cerro da Árvore) and Várzea do Capivarita Complex shared a tectonic evolution at 800–770 Ma. Based on Sr-Nd isotopes, this magmatism would have had a significant contribution from crustal materials (Battisti et al., 2023).

The small geochemical differences between the Piratini and Cerro Bori orthogneisses could be explained by the increasing maturity during arc evolution. Nevertheless, the Piratini and Cerro do Bori orthogneiss are exposed on the eastern border of the Pelotas-Aiguá Batholith as xenoliths. To the west and separated from the Pelotas Batholith by the Dorsal de Canguçu shear zone, the Porongos Complex metavolcanic rocks are exposed. Therefore, the dispersal character of these units along distinct crustal blocks separated by the Dorsal de Canguçu shear zone requires a careful evaluation of the single arc hypothesis, especially because of the limited amount of data about the Tonian relicts.

Alternatively, a rift setting was suggested for those Tonian relicts (Saalman et al., 2006; Konopásek et al., 2018; Will et al., 2020). In this view, the Tonian igneous rocks had a syn-sedimentary origin, and the geochemical arc signature would be inherited from older sources (Konopásek et al., 2018). This hypothesis cannot be ruled out. However, the data presented here do not support a rift origin. Besides, in the studied area, no evidence of syn-sedimentary volcanism was identified, and there are no indications of bimodal magmatism in the Porongos Complex. Therefore, in this study, as previously discussed, we interpret the geochemical signatures of the protoliths of the Godinho antiform metavolcanic rocks as evidence of origin in a Tonian arc setting.

The metavolcanic rocks of the Godinho antiform show 1.7–2.2 Ga T_{DM} ages, negative ϵ_{Hf} signatures, and Paleo- to Mesoproterozoic inherited zircons (2.2–1.1 Ga) (Pertille et al., 2017). The isotopic data and the inherited zircon grains require a Paleo- to Mesoproterozoic basement for this arc magmatism. The Encantadas and Arroio dos Ratos complexes could represent this basement, but the lack of Mesoproterozoic ages in these units makes it a debatable issue (inherited zircons \sim 1.1 Ga). Mesoproterozoic zircon grains were identified in the clastic metasedimentary rocks of the Porongos Complex (Gruber et al., 2011; Pertille et al., 2017), and the sources could be related to the Namaqua Belt (e.g., Konopásek et al., 2018) or the Sunsás orogenies. Nevertheless, in all proposed tectonic reconstructions of Tonian age, the extension and position of the Paleo- to Mesoproterozoic crust are arguable, as well as the subduction direction.

Assuming the earlier Porongos paleo-basin as a passive margin (e.g., Jost and Bitencourt, 1980; Camozzato et al., 2017), the Tonian magmatic arc would be formed by tectonic inversion with eastward or westward subduction or in an adjacent magmatic arc interleaved in the earlier basin. In this scenario, some hypotheses include a back-arc setting related to the Dom Feliciano arc (Camozzato et al., 2017), a forearc setting of the Piratini arc (Vieira et al., 2019), or another arc that could be partially reworked in the main collisional event between the Rio de La Plata and Kalahari cratons.

In summary, the presented data allows us to include the metavolcanic rocks of the Godinho antiform in the Tonian timeframe discussion. Their complex structural pattern includes ductile to semi-ductile deformational phases. The earlier ductile phase D_1 is marked by a non-mylonitic and mylonitic foliation (S_1) associated with the main thrust event of the Porongos Complex. These deformational phases were accompanied by greenschist metamorphism. Although detailed regional mapping and isotopic data are required for further tectonic interpretations, this study presents the first approach to metavolcanic rocks of the Godinho antiform and reveals significant information about this poorly understood unit.

CONCLUSIONS

The Porongos Complex is a fold and thrust belt that comprises distinct and intercalated units formed in different geotectonic contexts. In this study, we present new data for the metavolcanic rocks of the Godinho antiform that contributes to the recent discussion of the geological setting responsible for the formation of these rocks. The following conclusions are drawn based on the integrated methodology presented in this study and the literature data:

- The protoliths of the metavolcanic rocks of the Godinho antiform were geochemically discriminated as rhyodacite to dacite with calc-alkaline and peraluminous characters.
- The geochemical signature of the studied metavolcanic rocks from the Godinho antiform suggests a continental arc setting.
- According to the geochemical data, the studied metavolcanic rocks are similar to the metavolcanic rocks of the Cerro da Árvore Complex, Várzea do Capivarita orthogneisses, Piratini orthogneisses, and Cerro Bori orthogneisses.
- The structural investigation of the Godinho antiform enabled the identification of two ductile and one semi-ductile deformational phases generated during the Brasiliano event.
- The first detailed mineral characterization of the metavolcanic rocks of the Godinho antiform presented in this study enables the proposition of a widespread greenschist facies metamorphism characterized by phengite + chlorite + clinozoisite-epidote + albite + quartz \pm actinolite mineral assemblages. This assemblage, combined with textural criteria and temperatures obtained using chlorite geothermometry (316°C on average), reinforces the greenschist facies conditions for these rocks.
- The metavolcanic rocks of the Godinho antiform originated in a continental magmatic arc environment and deformed along tangential shear zones during the Brasiliano event.

ACKNOWLEDGMENTS

We would like to thank Prof. Nilson Botelho and Prof. Tiago Jalowitzki for their help and contributions to microprobe analysis. Thanks to Gabriel da Silva Pontes for his help with the geological map of the Sul-Riograndense shield. This investigation was supported financially through a scholarship to Rodrigo Antonio de Freitas Rodrigues by Fundação de Amparo a Pesquisa do Rio Grande de Sul (Nº: 18/2551-0000625-4) and a grant to Juliana Pertille da Silva by Conselho Nacional de Desenvolvimento Científico e Tecnológico of Brazil, Edital Universal-2018, Nº: 436073/2018-8.

REFERENCES

- Allmendinger, R. W., Cardozo, N., Fisher, D. M. (2012). *Structural geology algorithms: vectors and tensors in structural geology*. Cambridge: Cambridge University Press.
- Almeida, F. F. M., Hasuí, Y., Brito Neves, B. B., Fuck, R. A. (1981). Brazilian structural provinces: an introduction. *Earth Science Review*, 17(1-2), 1-29. [https://doi.org/10.1016/0012-8252\(81\)90003-9](https://doi.org/10.1016/0012-8252(81)90003-9)
- Armbruster, T., Bonazzi, P., Akasaka, M., Bermanec, V., Chopin, C., Gieré, R., Heuss-Assbichler, S., Liebscher, A., Menchetti, S., Pan, Y., Pasero, M. (2006). Recommended nomenclature of epidote-group minerals. *European Journal of Mineralogy*, 18(5), 551-567. <https://doi.org/10.1127/0935-1221/2006/0018-0551>
- Auzanneau, E., Schmidt, M. W., Vielzeuf, D., Connolly, J. A. D. (2010). Titanium in phengite: a geobarometer for high temperature eclogites. *Contribution to Mineralogy and Petrology*, 159, 1-24. <https://doi.org/10.1007/s00410-009-0412-7>
- Bailey, E. H., Ragnarsdottir, K. V. (1994). Uranium and thorium solubilities in subduction zone fluids. *Earth and Planetary Science Letters*, 124(1-4), 119-129. [https://doi.org/10.1016/0012-821X\(94\)00071-9](https://doi.org/10.1016/0012-821X(94)00071-9)
- Baltatzis, E. (1987). Distribution of elements between coexisting phengite and chlorite from low grade rocks from Skiros Island, Greece. *Mineralogy and Petrology*, 37, 243-250. <https://doi.org/10.1007/BF01161819>
- Battisti, M. A. (2022). *Evolução geológica (800-560 Ma) do setor central do Cinturão Dom Feliciano com base no estudo petrológico e de proveniência dos complexos Porongos, Várzea do Capivarita e Passo Feio, RS*. PhD Thesis. Porto Alegre: Instituto de Geociências, UFRGS, 280 p. Available at: <http://hdl.handle.net/10183/239719>. Accessed on: Jul 5, 2023.
- Battisti, M. A., Bitencourt, M. F., De Toni, G. B., Nardi, L. V. S., Konopásek, J. (2018). Metavolcanic rocks and orthogneisses from Porongos and Várzea do Capivarita complexes: A case for identification of tectonic interleaving at different crustal levels from structural and geochemical data in southernmost Brazil. *Journal of South American Earth Science*, 88, 253-274. <https://doi.org/10.1016/j.jsames.2018.08.009>
- Battisti, M. A., Bitencourt, M. F., Florisbal, L. M., Nardi, L. V. S., Ackerman, L., Sláma, J., Padilha, D. F. (2023). Unravelling major magmatic episodes from metamorphic sequences of the Dom Feliciano Belt central sector, southernmost Brazil – A comparative study of geochronology, elemental geochemistry, and Sr-Nd data. *Precambrian Research*, 385, 106951. <https://doi.org/10.1016/j.precamres.2022.106951>
- Bourdelle, F., Parra, T., Chopin, C., Beyssac, C. (2013). A new chlorite geothermometer for diagenetic to low-grade metamorphic conditions. *Contribution to Mineralogy and Petrology*, 165, 723-735. <https://doi.org/10.1007/s00410-012-0832-7>
- Boyton, W. V. (1984). Geochemistry of rare earth elements: meteorite studies. In: Henderson, P. (ed.). *Rare Earth Element Geochemistry*. New York: Elsevier, 63 p.
- Brenan, J. M., Shaw, H. F., Ryerson, F. J., Phinney, D. L. (1995). Mineral-aqueous fluid partitioning of trace elements at 900°C and 2.0 GPa: constraints on the trace element chemistry of mantle and deep crustal fluids. *Geochimica et Cosmochimica Acta*, 59(16), 3331-3350. [https://doi.org/10.1016/0016-7037\(95\)00215-L](https://doi.org/10.1016/0016-7037(95)00215-L)
- Bruto Neves, B. B., Fuck, R. A., Pimentel, M. M. (2014). The Brasiliano collage in South America: a review. *Brazilian Journal of Geology*, 44(3), 493-518. <https://doi.org/10.5327/Z2317-4889201400030010>
- Brown, G. C., Thorpe, R. S., Webb, P. C. (1984). The geochemical characteristics of granitoids in contrasting arcs and comments on magma sources. *Journal of Geological Society of London*, 141(3), 413-426. <https://doi.org/10.1144/gsjgs.141.3.0413>
- Cabanis, B., Lecolle, M. (1989). Le diagramme La/10-Y/15-Nb/8: unoutil pour la discrimination de las series volcaniques et la mise em evidence des processus de mélange et/ou dès contamination crustal. *Comptes rendus de l'Académie des Sciences*, 309(2), 2023-2029. Available at: <http://pascal-francis.inist.fr/vibad/index.php?action=getRecordDetail&idt=6648552>. Accessed on: May 31, 2023.
- Camozzato, E., Lopes, R. C., Philipp, R. P. (2017). *Geologia e recursos minerais da folha Hulha Negra, SH.22-Y-C-I*. Escala 1:100.000, estado do Rio Grande do Sul. Porto Alegre: Programa Geologia do Brasil, CPRM. 164 p. Available at: <http://rigeo.cprm.gov.br/jspui/handle/doc/19253>. Accessed on: May 31, 2023.
- Cardozo, N., Allmendinger, R. W. (2013). Spherical projections with OSXStereonet. *Computers & Geosciences*, 51, 193-205. <https://doi.org/10.1016/j.cageo.2012.07.021>

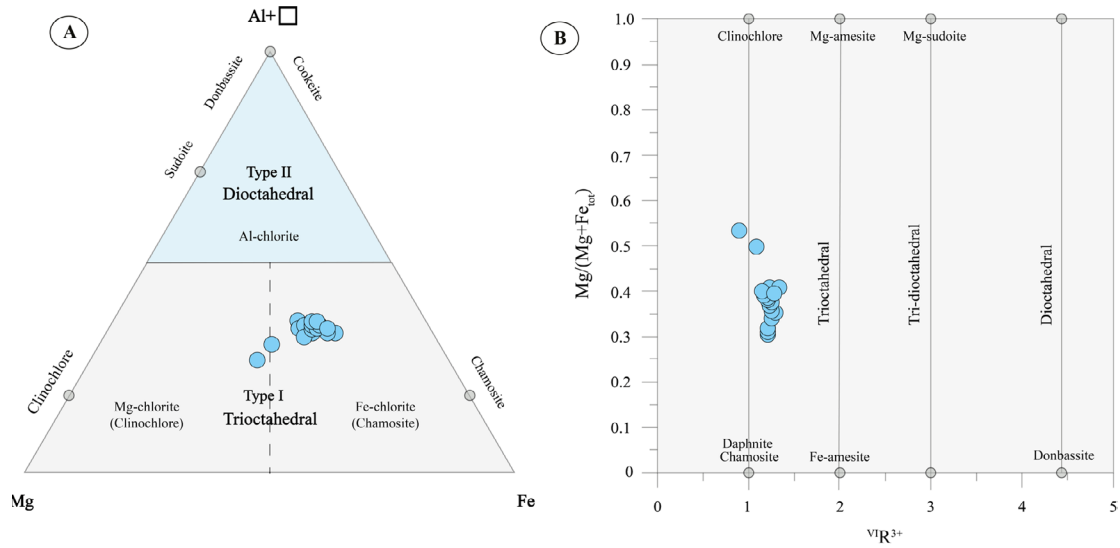
- Cathelineau, M. (1988). Cation site occupancy in chlorites and illites as function of temperature. *Clay Minerals*, 23(4), 471-485. <https://doi.org/10.1180/claymin.1988.023.4.13>
- Cerva-Alves, T., Hartmann, L. A., Remus, M. V. D., Lana, C. (2020). Integrated ophiolite and arc evolution, southern Brasileiro Orogen. *Precambrian Research*, 341, 105648. <https://doi.org/10.1016/j.precamres.2020.105648>
- Chinchilla, D., Arroyo, X., Merinero, R., Piña, R., Nieto, F., Ortega, L., Lunar, R. (2016). Chlorite Geothermometry applied to massive and oscillatory-zoned radiated Mn-rich chlorites in the Patricia Zn-Pb-Ag epithermal deposit (NE, Chile). *Applied Clay Science*, 134(Part 3), 210-220. <https://doi.org/10.1016/j.clay.2016.10.013>
- Coira, B., Kay, M., Viramonte, J. (1993). Upper Cenozoic magmatic evolution of the Argentine Puna – A model for changing subduction geometry. *International Geology Review*, 35(8), 677-720. <https://doi.org/10.1080/00206819309465552>
- Condie, K. C., Kröner, A. (2013). The building blocks of continental crust: Evidence for a major change in the tectonic setting of continental growth at the end of the Archean. *Gondwana Research*, 23(2), 394-402. <https://doi.org/10.1016/j.gr.2011.09.011>
- De Caritat, P., Hutcheon, I., Walshe, J.L. (1993). Chlorite Geothermometry: a review. *Clay Mineral*, 41, 219-239. <https://doi.org/10.1346/CCMN.1993.0410210>
- Deer, W. A., Howie, R. A., Zussman, J. (2009). *Rock-Forming Minerals*. 2. ed. London: Geological Society of London. v. 3B. 314 p.
- De Toni, G. B., Bitencourt, M. F., Konopásek, J., Battisti, M. A., Costa, E. O., Savian, J. F. (2021). Autochthonous origin of the Encruzilhada Block, Dom Feliciano Belt, southern Brazil, based on aerogeophysics, image analysis and PT-paths. *Journal of Geodynamics*, 144, 101825. <https://doi.org/10.1016/j.jog.2021.101825>
- De Toni, G. B., Bitencourt, M. F., Nardi, L. V. S., Florisbal, L. M., Almeida, B. S., Geraldés, M. (2020). Dom Feliciano Belt orogenic cycle tracked by its pre-collisional magmatism: the Tonian (ca. 800 Ma) Porto Belo Complex and its correlations in southern Brazil and Uruguay. *Precambrian Research*, 342, 105702. <https://doi.org/10.1016/j.precamres.2020.105702>
- Fernandes, L. A. D., Tommasi, A., Porcher, C. C. (1992). Deformation patterns in the southern Brazilian branch of the Dom Feliciano Belt: A reappraisal. *Journal of South American Earth Science*, 5(1), 77-96. [https://doi.org/10.1016/0895-9811\(92\)90061-3](https://doi.org/10.1016/0895-9811(92)90061-3)
- Fleuty, M. J. (1964). The description of folds. *Proceedings of the Geologists' Association*, 75(4), 461-492. [https://doi.org/10.1016/S0016-7878\(64\)80023-7](https://doi.org/10.1016/S0016-7878(64)80023-7)
- Fragoso-César, A. R. S. (1991). *Tectônica de placas no Ciclo Brasileiro: as orogenias dos cinturões Dom Feliciano e Ribeira no Rio Grande do Sul*. Thesis (Doctoral). São Paulo: Instituto de Geociências – USP. <https://doi.org/10.11606/T.44.1991.tde-23042013-162133>
- Gill, R. (2010). *Igneous rocks and processes: a practical guide*. Hoboken: John Wiley and Sons.
- Gollmann, K., Marques, J. C., Frantz, J. C., Chemale Jr., F. (2008). Geoquímica e isótopos de Nd de rochas metavulcânicas da Antiforme Capané, Complexo Porongos, RS. *Revista Pesquisas em Geociências*, 35(2), 83-95. <https://doi.org/10.22456/1807-9806.17939>
- Gorton, M. P., Schandl, E. S. (2000). From continents to island arcs: a geochemical index of tectonic setting for arc-related and within-plate felsic to intermediate volcanic rocks. *The Canadian Mineralogist*, 38(5), 1065-1073. <https://doi.org/10.2113/gscanmin.38.5.1065>
- Gruber, L., Lenz, C., Porcher, C. C., Fernandes, L. A. D. (2011). Proveniência de metassedimentos das sequências Arroio Areião, Cerro Cambará e Quartzito Milonitos no Complexo Porongos, Santana da Boa Vista, RS. *Pesquisas em Geociências*, 38(3), 205-223. <https://doi.org/10.22456/1807-9806.35157>
- Gruber, L., Porcher, C. C., Koester, E., Bertotti, A. L., Lenz, C., Fernandes, L. A. D., Remus, M. V. D. (2016). Isotope geochemistry and geochronology of syn-depositional volcanism in Porongos metamorphic complex, Santana da Boa Vista Antiform, Dom Feliciano belt, Brazil: onset of an 800 Ma continental arc. *Journal of Sedimentary Environment*, 1(2), 96-215. <https://doi.org/10.12957/jse.2016.22722>
- Guidotti, C. V. (1984). Micas in metamorphic rocks. In: Bayler, B. W. (ed.). *Micas. Reviews in Mineralogy and Geochemistry*, 13, 357-468.
- Guidotti, C. V., Sassi, F. P. (1998). Miscellaneous isomorphous substitutions in Na-K white micas: a review, with special emphasis to metamorphic micas. *Rendiconti Lincei Scienze Fisiche e Naturali*, 9, 57-78. <https://doi.org/10.1007/BF02904456>

- Harris, N. B. W., Pearce, J. A., Tindle, A. G. (1986). Geochemical characteristics of collision-zone magmatism. *Geological Society, London, Special Publications*, 19(1), 67-81. <https://doi.org/10.1144/GSL.SP.1986.019.01.04>
- Hawkesworth, C. J., Gallagher, K., Hergt, J. M., McDermott, F. (1993). Mantle and slab contributions in arc magmas. *Annual Review of Earth and Planetary Sciences*, 21, 175-204. <https://doi.org/10.1146/annurev.earth.21.050193.001135>
- Hawkesworth, C. J., Turner, S. P., McDermott, F., Peate, D. W., Calsteren, P. V. (1997). U-Th isotopes in arc magmas: implications for element transfer from subducted crust. *Science*, 276(5312), 551-555. <https://doi.org/10.1126/science.276.5312.551>
- Höfig, D. F., Marques, J. C., Basei, M. A. S., Giusti, R. O., Kohlrausch, C., Frantz, J. C. (2018). Detrital zircon geochronology (U-Pb LA-ICP-MS) of syn-orogenic basins in SW Gondwana: new insights into the Cryogenian-Ediacaran of Porongos Complex, Dom Feliciano belt, southern Brazil. *Precambrian Research*, 306, 189-208. <https://doi.org/10.1016/j.precamres.2017.12.031>
- Inoue, A., Kurokawa, K., Hatta, T. (2010). Application of chlorite geothermometry to hydrothermal alteration in Toyoha geothermal system, southwestern Hokkaido, Japan. *Resource Geology*, 60(1), 52-70. <https://doi.org/10.1111/j.1751-3928.2010.00114.x>
- Ionov, D. A., Grégoire, M., Prikhod'ko, V. S. (1999). Feldspar-Ti-oxide metasomatism in off-cratonic continental and oceanic upper mantle. *Earth and Planetary Science Letters*, 165(1), 37-44. [https://doi.org/10.1016/S0012-821X\(98\)00253-2](https://doi.org/10.1016/S0012-821X(98)00253-2)
- Irvine, T. N., Baragar, W. R. A. (1971). A guide to the chemical classification of the common volcanic rocks. *Canadian Journal of Earth Science*, 8(5), 523-548. <https://doi.org/10.1139/e71-055>
- Jahn, B., Wu, F., Lo, C., Tsai, C. (1999). Crust-mantle interaction induced by deep subduction of the continental crust: geochemical and Sr-Nd isotopic evidence from post-collisional mafic-ultramafic intrusions of the northern Dabie complex, central China. *Chemical Geology*, 157(1-2), 119-146. [https://doi.org/10.1016/S0009-2541\(98\)00197-1](https://doi.org/10.1016/S0009-2541(98)00197-1)
- Jost, H., Bitencourt, M. F. (1980). Estratigrafia e tectônica de uma fração da faixa de dobramentos Tijucas no Rio Grande do Sul. *Acta Geologica Leopoldensia*, 4, 27-60.
- Jowett, E. C. 1991. Fitting iron magnesium into the hydrothermal chlorite geothermometer. In: Proceeding of the Program with Abstracts, Geological Association of Canada – Mineralogical Association of Canada. Society of Economic Geologists. 16, 62 p.
- Kendrick, J., Yakymchuk, C. (2020). Garnet fractionation, progressive melt loss and bulk composition variations in anatectic metabasites: complications for interpreting the geodynamic significance of TTGs. *Geoscience Frontiers*, 11(3), 745-763. <https://doi.org/10.1016/j.gsf.2019.12.001>
- Koester, E., Porcher, C. C., Pimentel, M. M., Fernandes, L. A. D., Vignol-Lelarge, M. L., Oliveira, L. D., Ramos, R. C. (2016). Further evidence of 777 Ma subduction-related continental arc magmatism in Eastern Dom Feliciano belt, southern Brazil: the Chácara das Pedras Orthogneisses. *Journal of South American Earth Science*, 68, 155-166. <https://doi.org/10.1016/j.jsames.2015.12.006>
- Konopásek, J., Janoušek, V., Oyhantçabal, P., Sláma, J., Ulrich, S. (2018). Did the circum-Rodinia subduction trigger the Neoproterozoic rifting along the Congo-Kalahari Craton margin? *International Journal of Earth Science*, 107, 1859-1894. <https://doi.org/10.1007/s00531-017-1576-4>
- Le Bas, M. J., Le Maitre, R. W., Streckeisen, A., Zanettin, B. (1986). A chemical classification of volcanic rocks based on total alkali silica diagram. *Journal of Petrology*, 27(3), 745-750. <https://doi.org/10.1093/petrology/27.3.745>
- Leite, J. A. D., Hartmann, L. A., McNaughton, N. J., Chemale, F. (1998). SHRIMP U-Pb zircon geochronology of Neoproterozoic Juvenile and Crustal-reworked Terranes in Southernmost Brazil. *International Geology Review*, 40(8), 688-705. <https://doi.org/10.1080/00206819809465232>
- Lena, L. O. F., Pimentel, M. M., Philipp, R. P., Armstrong, R., Sato, K. (2014). The evolution of the Neoproterozoic São Gabriel juvenile terrane, southern Brazil based on high spatial resolution U-Pb ages and $\delta^{18}\text{O}$ data from detrital zircons. *Precambrian Research*, 247, 126-138. <https://doi.org/10.1016/j.precamres.2014.03.010>
- Lenz, C. (2006). *Evolução metamórfica dos metapelitos da Antiforme Serra dos Pedras: condições e idades do metamorfismo*. Master's Thesis. Porto Alegre: Instituto de Geociências, UFRGS, 111 p. Available at: <http://hdl.handle.net/10183/8520>. Accessed on: Jul 5, 2023.
- Lenz, C., Fernandes, L. A. D., McNaughton, N. J., Porcher, C. C., Masquelin, H. (2011). U-Pb SHRIMP ages for the Cerro Bori orthogneisses, Dom Feliciano belt in Uruguay: evidences of a ~800 Ma magmatic and ~650 Ma metamorphic event. *Precambrian Research*, 185(3-4), 149-163. <https://doi.org/10.1016/j.precamres.2011.01.007>

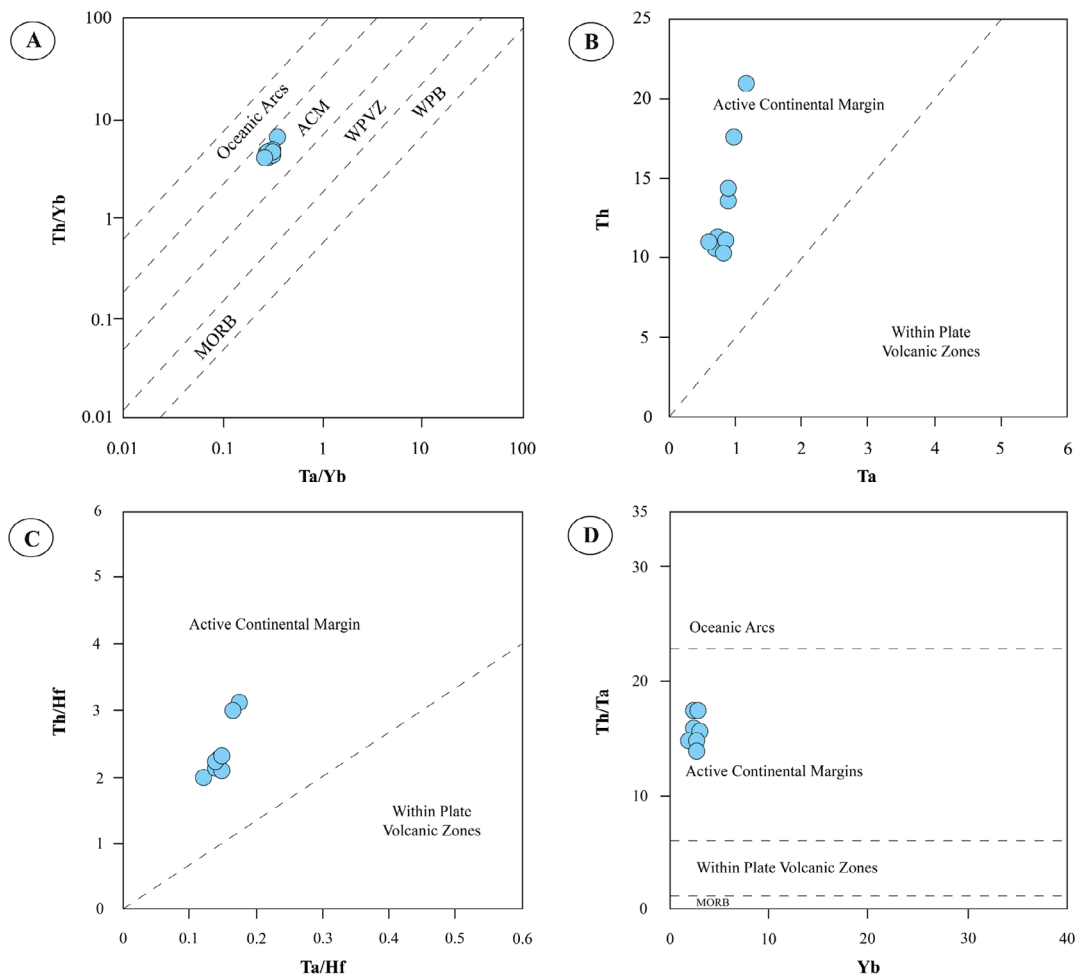
- Lenz, C., Porcher, C. C., Fernandes, L. A. D., Masquelin, H., Koester, E., Conceição, R. V. (2013). Geochemistry of the Neoproterozoic (800-767 Ma) Cerro Bori orthogneisses, Dom Feliciano belt, in Uruguay: Tectonic evolution of an ancient continental arc. *Mineralogy and Petrology*, 107, 785-806. <https://doi.org/10.1007/s00710-012-0244-4>
- Li, G., Peacor, D. R., Coombs, D. S., Kawachi, Y. (1997). Solid solution in the celadonite family: The new minerals ferroceldonite, $K_2Fe^{2+}_2Fe^{3+}_2Si_8O_{20}(OH)_4$, and ferroaluminoceldonite, $K_2Fe^{2+}_2Al_2Si_8O_{20}(OH)_4$. *American Mineralogist*, 82(5-6), 503-511. <https://doi.org/10.2138/am-1997-5-609>
- Lusa, M., Philipp, R. P., Nardi, L. V. S. (2010). Geoquímica e petrologia dos metagranitos do Complexo Encantadas, Santana da Boa Vista, (RS): a evolução de uma margem continental ativa no Paleoproterozóico. *Revista Brasileira de Geociências*, 40(2), 151-166.
- Martil, M. M. D., Bitencourt, M. F., Nardi, L. V. S. (2011). Caracterização Estrutural e petrológica do magmatismo pré-colisional do Escudo Sul-rio-grandense: os ortogneisses do Complexo Metamórfico Várzea do Capivarita. *Pesquisas em Geociências*, 38(2), 181-201. <https://doi.org/10.22456/1807-9806.26383>
- Martil, M. M. D., Bitencourt, M. F., Nardi, L. V. S., Schmitt, R. S., Weinberg, R. (2017). Pre-collisional, Tonian (ca. 790 Ma) continental arc magmatism in southern Mantiqueira Province, Brazil: geochemical and isotopic constraints from the Várzea do Capivarita Complex. *Lithos*, 274-275, 39-52. <https://doi.org/10.1016/j.lithos.2016.11.011>
- McDonough, W. F., Sun, S.-S. (1995). The composition of the Earth. *Chemical Geology*, 120(3-4), 223-253. [https://doi.org/10.1016/0009-2541\(94\)00140-4](https://doi.org/10.1016/0009-2541(94)00140-4)
- Moazzen, M. (2004). Chlorite-chloritoid-garnet equilibria and geothermobarometry in the Sanandaj-Sirjan metamorphic belt, southern Iran. *Iranian Journal Science and Technology Transaction*, 28, 65-78.
- Oriolo, S., Oyhantçabal, P., Wemmer, K., Siegesmund, S. (2017). Contemporaneous assembly of Western Gondwana and final Rodinia break-up: implications for the supercontinent cycle. *Geoscience Frontiers*, 8(6), 1431-1445. <https://doi.org/10.1016/j.gsf.2017.01.009>
- Passchier, C. W., Trouw, R. A. J. (2005). *Microtectonics*. 2ª ed. Berlin: Springer.
- Pearce, J. A. (1996). Sources and settings of granitic rocks. *Episodes*, 19(4), 120-125. <https://doi.org/10.18814/epiiugs/1996/v19i4/005>
- Pearce, J. A. (2008). Geochemical fingerprinting of oceanic basalts with applications to ophiolite classification and the search for Archean oceanic crust. *Lithos*, 100(1-4), 14-48. <https://doi.org/10.1016/j.lithos.2007.06.016>
- Pearce, J. A., Harris, N. B. W., Tindle, A. G. (1984). Trace element distribution diagrams for the tectonic interpretation of granitic rocks. *Journal of Petrology*, 25(4), 956-983. <https://doi.org/10.1093/ptrology/25.4.956>
- Pearce, M. A., Wheeler, J. (2014). Microstructural and metamorphic constraints on the thermal evolution of the southern region of the Lewisian Gneiss Complex, NW Scotland. *Journal of Petrology*, 55(10), 2043-2066. <https://doi.org/10.1093/ptrology/egu049>
- Peccerillo, A., Taylor, S. R. (1976). Geochemistry of Eocene calc-alkaline volcanic rocks from the Kastamonu area, Northern Turkey. *Contribution to Mineralogy and Petrology*, 58, 63-81. <https://doi.org/10.1007/BF00384745>
- Pertille, J., Hartmann, L. A., Philipp, R. P. (2015a). Zircon U-Pb age constraints on the Paleoproterozoic sedimentary basement of the Ediacaran Porongos Group, Sul-Riograndense Shield, southern Brazil. *Journal of South American Earth Sciences*, 63, 334-345. <https://doi.org/10.1016/j.jsames.2015.08.005>
- Pertille, J., Hartmann, L. A., Philipp, R. P., Petry, T. S., Carvalho Lana, C. (2015b). Origin of the Ediacaran Porongos Group, Dom Feliciano belt, southern Brazilian shield, with emphasis on whole rock and detrital zircon geochemistry and U-Pb, Lu-Hf isotopes. *Journal of South American Earth Sciences*, 64(Part 1), 69-93. <https://doi.org/10.1016/j.jsames.2015.09.001>
- Pertille, J., Hartmann, L. A., Santos, J. O. S., McNaughton, N. J., Armstrong, R. (2017). Reconstructing the Cryogenian-Ediacaran evolution of the Porongos fold and thrust belt, Southern Brasiliano Orogen, based on Zircon U-Pb-Hf-O isotopes. *International Geology Review*, 59(12), 1532-1560. <https://doi.org/10.1080/00206814.2017.1285257>
- Philipp, R. P., Campos, R. S. (2004). Geologia, Petrografia e litogeoquímica dos Gnaisses Porto Alegre, RS, Brasil: implicações geotectônicas. *Pesquisas em Geociências*, 31(2), 79-94. <https://doi.org/10.22456/1807-9806.19575>
- Philipp, R. P., Lusa, M., Nardi, L. V. S. (2008). Geochemistry and petrology of dioritic, tonalitic and trondhjemitic gneisses from Encantadas Complex, Santana da Boa Vista, southernmost Brazil: Paleoproterozoic continental-arc magmatism. *Anais da Academia Brasileira de Ciências*, 80(4), 735-748. <https://doi.org/10.1590/S0001-37652008000400013>

- Philipp, R. P., Pimentel, M. M., Chemale Jr., F. (2016). Tectonic evolution of the Dom Feliciano belt in southern Brazil: geological relationships and U-Pb geochronology. *Brazilian Journal of Geology*, 46(Suppl. 1), 83-104. <https://doi.org/10.1590/2317-4889201620150016>
- Plissart, G., F erm enias, O., M aruntiu, M., Diot, H., Demaiffe, D. (2009). Mineralogy and Geothermometry of gabbro-derived listvenites in the Tisovita-luti ophiolite, southwestern Romania. *Canadian Mineralogist*, 47, 81-105.
- Porcher, C. C. (1992). *Caracteriza  o das condi  es de fluxo de uma zona de cisalhamento tangencial na regi  o de Santana da Boa Vista (RS)*. Dissertation (Master). Porto Alegre: Universidade Federal do Rio Grande do Sul, 192 p.
- Porcher, C. C., Fernandes, L. A. D. (1990). Rela  es embasamento/cobertura na por  o ocidental do Cintur  o Dom Feliciano: um esbo  o estrutural. *Pesquisas em Geoci  ncias*, 17(1-2), 72-84. <https://doi.org/10.22456/1807-9806.21384>
- Ramos, R. C., Koester, E., Vieira, D. T., Porcher, C. C., Gezatt, J. N., Silveira, R. L. (2018). Insights on the evolution of the Arroio Grande ophiolite (Dom Feliciano belt, Brazil) from Rb-Sr and SHRIMP U-Pb isotopic geochemistry. *Journal of South American Earth Sciences*, 86, 38-53. <https://doi.org/10.1016/j.jsames.2018.06.004>
- Remus, M. V. D., Hartmann, L. A., Ribeiro, M. (1991). Nota sobre a geologia dos metamorfitos de press  o intermedi  ria e granit  ides associados da regi  o de Pinheiro Machado/RS. *Acta Geologica Leopoldensia*, 34, 175-190.
- Rieder, M., Cavazzini, G., D'yakonov, Y. S., Frank-Kamenetskii, V. A., Gottardi, G., Guggenheim, S., Koval, P. V., M uller, G., Neiva, A. M. R., Radoslovich, E. W., Robert, J. L., Sassi, F. P., Takeda, H., Weiss, Z., Wones, D. (1998). Nomenclature of the Micas. *Clays and Clay Minerals*, 46(5), 586-595. <https://doi.org/10.1346/CCMN.1998.0460513>
- Rudnick, R. L., Gao, S. (2003). Composition of the continental crust. In: Holland, H. D., Turekian, K. K. (eds.). *Treatise on Geochemistry*. Oxford: Elsevier. v. 3. p. 1-64.
- Saalmann, K., Gerdes, A., Lahaye, Y., Hartmann, L. A., Remus, M. V. D., L aufer, A. (2011). Multiple accretion at the eastern margin of the Rio de la Plata craton: the prolonged Brasiliano orogeny in southernmost Brazil. *International Journal of Earth Science*, 100, 355-378. <https://doi.org/10.1007/s00531-010-0564-8>
- Saalmann, K., Hartmann, L. A., Remus, M. (2005). Tectonic evolution of two contrasting schist belts in southernmost Brazil: a plate tectonic model for the Brasiliano orogeny. *International Geology Review*, 47(12), 1234-1259. <https://doi.org/10.2747/0020-6814.47.12.1234>
- Saalmann, K., Remus, M. V. D., Hartmann, L. A. (2006). Structural evolution and tectonic setting of the Porongos belt, southern Brazil. *Geological Magazine*, 143(1), 59-88. <https://doi.org/10.1017/S0016756805001433>
- Santos, J. O. S., Hartmann, L. A., Bossi, J., Campal, N., Schipilov, A., Pi neyro, D., McNaughton, N. J. (2003). Duration of the Trans-Amazonian Cycle and its correlation within South America Based on U-Pb SHRIMP Geochronology of the La Plata Craton, Uruguay. *International Geology Review*, 45(1), 27-48. <https://doi.org/10.2747/0020-6814.45.1.27>
- Schandl, E. S., Gorton, M. P. (2002). Application of high field strength elements to discriminate tectonic setting in VMS environments. *Economic Geology*, 97(3), 629-642. <https://doi.org/10.2113/gsecongeo.97.3.629>
- Schmidt, R., Franz, L., Oberh ansli, R., Dong, S. (2000). High-Si phengite, mineral chemistry and P-T evolution of ultra-high-pressure eclogites and calc-silicates from the Dabie Shan, eastern China. *Geological Journal*, 35(3-4), 185-207. <https://doi.org/10.1002/gj.863>
- Silva, L. C., Hartmann, L. A., McNaughton, N. J., Fletcher, I. R. (1999). SHRIMP U-Pb zircon dating of Neoproterozoic Granitic Magmatism and Collision in the Pelotas Batholith, Southernmost Brazil. *International Geology Review*, 41(6), 531-551. <https://doi.org/10.1080/00206819909465156>
- Stern, R. J. (2002). Subduction zones. *Reviews of Geophysics*, 40(4), 31-38. <https://doi.org/10.1029/2001RG000108>
- Takehara, L., Laux, J. H. (2019). * rea de relevante interesse mineral: integra  o geol gica-geof sica e recursos minerais Bat olito Pelotas e Terreno Tijucas. Escala 1:500.000, estado do Rio Grande do Sul*. Porto Alegre: CPRM, 186 p.
- Tambara, G. B. (2015). *Gnaisses Piratini: Magmatismo de 784 Ma no Sudeste do Cintur  o Dom Feliciano*. Dissertation (Master). Porto Alegre: Instituto de Geoci  ncias – UFRGS.
- Tambara, G. B., Koester, E., Ramos, R. C., Porcher, C. C., Vieira, D. T., Fernandes, L. A. D., Lenz, C. (2019). Geoqu mica e geocronologia dos Gnaisses Piratini: magmatismo c lcio-alcalino m dio a alto-K de 784 Ma (U-Pb SHRIMP) no SE do Cintur  o Dom Feliciano (RS, Brasil). *Pesquisas em Geoci  ncias*, 46(2), e0769. <https://doi.org/10.22456/1807-9806.95466>

- Tappert, M. C., Rivard, B., Giles, D., Tappert, R., Mauger, A. (2013). The mineral chemistry, near-infrared, and mid-infrared reflectance spectroscopy of phengite from the Olympic Dam IOCG deposit, South Australia. *Ore Geology Reviews*, 53, 26-38. <https://doi.org/10.1016/j.oregeorev.2012.12.006>
- Trincal, V., Lanari, P., Buatier, M., Lacroix, B., Charpentier, D., Labaume, P., Muñoz, M. (2015). Temperature micro-mapping in oscillatory-zoned chlorite: Application to study of a green-schist facies fault zone in the Pyrenean Azial Zone (Spain). *American Mineralogist*, 100(11-12), 2468-2483. <https://doi.org/10.2138/am-2015-5217>
- Vidal, O., De Andrade, V., Lewin, E., Munoz, M., Parra, T., Pascarelli, S. (2006). P-T-deformation-Fe³⁺/Fe²⁺ mapping at the thin section scale and comparison with XANES mapping: application to a garnet-bearing metapelite from the Sambagawa metamorphic belt (Japan). *Journal of Metamorphic Geology*, 24(7), 669-683. <https://doi.org/10.1111/j.1525-1314.2006.00661.x>
- Vieira, D. T., Koester, E., Ramos, R. C., Porcher, C. C. (2019). Sr-Nd-Hf isotopic constraints and U-Pb geochronology of the Arroio Pedrado Gneisses, Dom Feliciano belt, Brazil: A 680 Ma shoshonitic event in the final stages of the Piratini Arc evolution. *Journal of South American Earth Sciences*, 95, 102294. <https://doi.org/10.1016/j.jsames.2019.102294>
- Wilson, M. S. (1989). Igneous petrogenesis A global tectonic approach. London: Chapman and Hall. 466 p. <https://doi.org/10.1007/978-1-4020-6788-4>
- Will, T. M., Höhn, S., Frimmel, H. E., Gaucher, C., le Roux, P. J., Macey, P. H. (2020). Petrological, geochemical and isotopic data of Neoproterozoic rock units from Uruguay and South Africa: Correlation of basement terranes across the South Atlantic. *Gondwana Research*, 80, 12-32. <https://doi.org/10.1016/j.gr.2019.10.012>
- Winchester, J. A., Floyd, P. A. (1977). Geochemical discrimination of different magma series and their differentiation products using immobile elements. *Chemical Geology*, 20, 325-343. [https://doi.org/10.1016/0009-2541\(77\)90057-2](https://doi.org/10.1016/0009-2541(77)90057-2)
- Wise, W. S., Eugster, H. P. (1964). Celadonite: synthesis, thermal stability and occurrence. *American Mineralogist*, 49(7-8), 1031-1083.
- Yavuz, F., Kumral, M., Karakaya, N., Karakaya, M. Ç., Yildirim, D. (2015). A Windows program for chlorite calculation and classification. *Computers & Geosciences*, 81, 101-113. <https://doi.org/10.1016/j.cageo.2015.04.011>
- Yavuz, F., Yildirim, D. K. (2018). A windows program for calculation and classification of epidote-supergroup minerals. *Periodico di Mineralogia*, 87(3), 269-285. <https://doi.org/10.2451/2018PM808>
- Zane, A., Weiss, Z. (1998). A procedure for classifying rock-forming chlorites based on microprobe data. *Rendiconti Lincei*, 9, 51-56. <https://doi.org/10.1007/BF02904455>



Annex 1. (A) Compositional diagram for chlorite classification based on values of Al+□–Mg–Fe (Zane and Weiss, 1998). (B) Chlorite classification diagram Mg/(Mg+Fe_{tot}) versus V¹R³⁺ (apfu) (Plissart et al., 2009).



Annex 2. Geotectonic discrimination diagrams used for classification of the metavolcanic rocks of Godinho antiform. Th/Yb-Ta/Yb, Th-Ta, Th/Hf-Ta/Hf, and Th/Ta-Yb, diagrams after Schandl and Gorton (2002).